Lund University

Interfaces in complex InAs-GaSb heterostructured nanowires - A transmission electron microscopy study

Author:
Louise Gren

Supervisor:
Reza Zamani

February 16, 2017

Lund
University

Abstract

In this project epitaxially grown InAs-GaSb complex heterostructured nanowires have been characterized by means of aberration corrected TEM techniques and energy dispersive X-ray spectroscopy (EDX). The InAs-GaSb material is of interest due to its high charge carrier mobility, which has possible applications in electronic devices such as FETs. InAs-GaSb heterostructured nanowires in zincblende structure have previously been studied and have possible electronic applications such as tunneling field effect transistors. However, heterostructured nanowires of InAs-GaSb in wurtzite structure have until now not been observed. The focus of this project have been to perform a structural characterization of InAs-GaSb core-shell and InAs-GaSb-InAs core-shell-shell nanowires with an emphasis on the interfaces. Epitaxial axial growths of GaSb are present on top of the core-shell(-shell) structures which are induced by the seed particles during the shell growth.

The lattice mismatch of wurtzite InAs-GaSb is 1.15%. However, the nanowire shells were fully epitaxial with practically no misfit dislocations. This is due to that the elastic relaxation mechanisms are the dominating mechanisms for compensating the lattice mismatch induced strain. As the shells were fully epitaxial stacking faults are transferred from the core to the shells. The tapering events of the shells were found to generally coincide with these stacking faults.

Analysis with high resolution EDX revealed a change of composition at the axial interface between the InAs core and the axial growth of GaSb. A short segment, $\sim$6 nm, of GaAsSb ternary at the axial interface is attributed to the different solubility of the elements in the Au seed particle and to the reservoir effect of the seed particle during epitaxial growth.

A one atomic bilayer thick composition change was present at the radial interfaces, which was observed by means of aberration corrected scanning TEM (STEM). The bilayer was a ternary of InAsGa between the InAs core and the GaSb shell. Such bilayers were present also at both interfaces in the GaSb-InAs double shell nanowires. This change in composition might influence the band gap alignment and subsequently the electric properties of the material. It is of importance to further evaluate the functional impact of this ternary in order to further understand and develop core-shell materials. Evidence of metastability of the core-shell nanowires were also found during the project which is another important phenomenon to further investigate.

Acknowledgements

I would like to thank Dr. Reza Zamani for introducing me to the world of transmission electron microscopy and generously sharing his time and knowledge. I would also like to acknowledge Luna Namazi for providing me with interesting nanowires to characterize.

I would also like to thank the members of Prof. Kimberly Dick Thelanders group at Fasta Tillstandets Fysik for contributing to the progress of this project.

Prof. Per Persson and assistant Prof. Magnus Garbrecht I would like to thank for the collaboration and welcoming us to Linköping University and Angströmshuset. Nevertheless for allowing and helping us to use their aberration corrected S/TEM.

Last but not least I would like to thank the master students which I shared an office with for all the cookies and support.

Contents

1 Introduction **1**
- 1.1 Basic concepts . . . 2
  - 1.1.1 Semiconductors . . . 2
  - 1.1.2 Semiconductor devices . . . 3
  - 1.1.3 Nanowires and the growth mechanism . . . 3
  - 1.1.4 Crystal structures and physical properties . . . 4
  - 1.1.5 Growth of lattice-mismatched heterostructures . . . 8
- 1.2 The InAs-GaSb system . . . 9
- 1.3 Transmission electron microscopy . . . 10

2 Methodology **11**
- 2.1 The transmission electron microscope . . . 11
  - 2.1.1 The illumination system . . . 11
  - 2.1.2 The objective lenses and the sample stage . . . 12
  - 2.1.3 The imaging system . . . 13
- 2.2 Concepts . . . 13
  - 2.2.1 Electron-matter interaction . . . 13
  - 2.2.2 The concept of resolution . . . 14
  - 2.2.3 Aberrations . . . 16
  - 2.2.4 Contrast . . . 17
  - 2.2.5 Diffraction . . . 18
- 2.3 Methods . . . 19
  - 2.3.1 Conventional TEM (CTEM) . . . 19
  - 2.3.2 High resolution TEM (HRTEM) . . . 19
  - 2.3.3 Scanning TEM (STEM) imaging . . . 20
  - 2.3.4 Aberration corrected TEM and STEM . . . 20
- 2.4 Spectroscopy . . . 21
  - 2.4.1 Energy dispersive X-ray spectroscopy (EDX) . . . 21
- 2.5 Post-experiment data treatment . . . 22

3 Experimental procedures **24**
- 3.1 Material synthesis . . . 24
- 3.2 Electron microscopy . . . 25
- 3.3 Post-experiment data treatment and micrograph analysis . . . 25

4 Result and Discussion **26**
- 4.1 InAs-GaSb (WZ-ZB) core-shell nanowires (Sample A) . . . 27
- 4.2 InAs-GaSb (WZ-ZB-WZ) core-shell nanowires (Sample B) . . . 28
- 4.3 InAs-GaSb core- (thin) shell nanowires . . . 30
  - 4.3.1 Stacking faults . . . 30
  - 4.3.2 Morphology of the shell . . . 32
  - 4.3.3 The radial interface . . . 36
  - 4.3.4 The axial interface . . . 37
- 4.4 InAs-GaSb core-(thick) shell nanowires . . . 40

4.4.1 Morphology of the shell . . . 40
4.5 InAs-GaSb-InAs core-shell-shell nanowires . . . 42
4.5.1 Morphology of the shell . . . 43
4.5.2 The radial interface . . . 47
4.5.3 The polycrystalline areas . . . 50

5 Conclusion **52**
5.1 Outlook . . . 53

A Phase contrast **54**
A.0.1 The contrast transfer function (CTF) . . . 54
A.0.2 Phase contrast function (pCTF) . . . 55

Bibliography **57**

Chapter 1

Introduction

Nanotechnology is a concept encompassing a wide area of applications which are related to many different fields such as electronics, biology, chemistry, physics etc. The very definition of a nanostructure is that at least one dimension of the structure in question is between 1 and 100 nm. The small size changes the properties of a material, and quantum confinement and low dimensionality phenomena become important concepts [1]. Nanowires are 1-dimensional structures exhibiting these phenomena which deviate from the same material properties in conventional bulk or thin films. An illustration of different nanowire structures is shown in figure 1.1. Research of nanowires is of interest as they have many potential applications in electronics, optoelectronics and life science to mention a few.

The synthesis of semiconductor nanowires can be controlled to a high degree, in order to design the electronic and optoelectronic properties [2][3]. One approach in this context is to create heterostructures. The small dimension of nanowires does not only change the electrical properties of a material as mentioned, it also changes the physics of how a material takes form. These differences are for example the reason for why we see polytypism, which is the ability to form different crystal structures of the same compound in nanostructures but not in bulk materials. This is one advantage of creating nanosized heterostructures compared to bulk heterostructures. Another advantage is the possibility to create layered structures of compounds which are not compatible, by means of lattice-mismatch, in bulk structures. This increase the possible nanowire configurations as these phenomenona are also possible to control to a high extent. This is important as the properties of the heterostructures are extremely sensitive to the crystal structure and chemical composition at the nanoscale.

As nanowires have two dimensions of less than a few 100 nm, the structures cannot be investigated by the human eye or even by a conventional light microscope. The overall structure is important to observe as well as the atomic arrangement and chemical composition. This can be done by state-of-the art electron microscopy and in particular transmission electron microscopes (TEM). It is of high importance to perform an extensive analysis to understand the relation between growth dynamics of the nanowire and the outcome structures. This will improve the nanowire synthesis and leads to obtaining the desired properties and consequently to better semiconductor devices.

The material of interest in this thesis is InAs-GaSb. The InAs-GaSb material is of interest due to its high charge carrier mobility, which has possible applications in electronic devices such as field effect transistors (FETs). Nanowires of InAs-GaSb in zincblende structure is well represented in the literature, however, InAs-GaSb in wurtzite structure have until now been unknown.

The objective of this thesis is to characterize these heterostructured wurtzite InAs-GaSb nanowires by means of TEM. The structural properties of crystal structures and nanowires, as well as the synthesis technique need to be discussed in order to understand the result from this characterization.

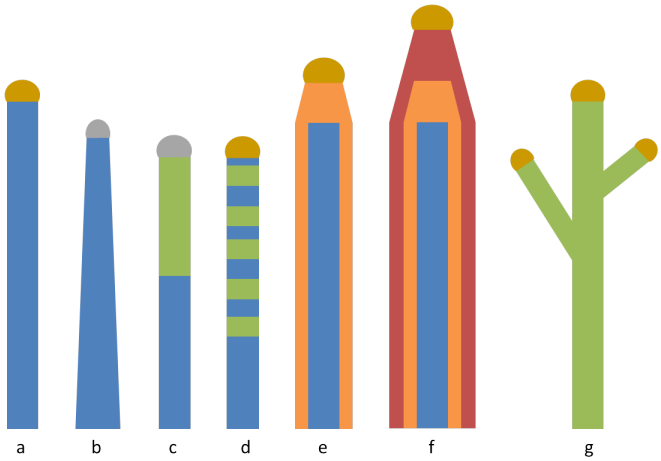

Figure 1.1: Nanowires can be produced (or synthesized or grown) in many different shapes and configurations. Some are illustrated (seeded bottom-up grown nanowires). The figure shows the cross-section of a (a) bare nanowire, (b) tapered bare nanowire, (c) axial heterostructure, (d) superlattice, (e) core-shell (radial heterostructure), (f) core-shell-shell or core-multishell and (g)a branched nanowire.

In this chapter will first basic concepts about semiconductors (and their heterostructures), the crystal structure of nanowires and the synthesis technique be described. Afterward, we will mention a brief background for the InAs-GaSb material system and then we will discuss the motivation for the instrumental choice of TEM.

1.1 Basic concepts

1.1.1 Semiconductors

A semiconductor is a material which can operate both as a conductor and an insulator, as its conducting properties can be altered by external forces. The characteristics of a semiconductor depend on its electronic states. The characteristic bandgap for a semiconductor is smaller than for an insulator, and if enough electrons have been excited to the conduction band it can start conduct current.

Thermal heating excite electrons in the valence band up to the conduction band [4]. The valence band is hence left with an equal amount of holes. The electrons and holes are charge carriers in the structure, and doping can be used to change the ratio of the two types in a material. The electronic states of a material also depend on the elemental composition, crystal structure, defects and the presence of doping atoms. It is of interest to be able to design the electronic states by altering the material in order to achieve a semiconductor with the desired optical or electrical characteristics. These properties can be further engineered by combining two semiconductor materials or phases. These kind of structures are the so-called heterostructure.

1.1.1.1 Heterostructures

The band gap characteristic of a semiconductor is material dependent. A heterojunction is created in the interface of two materials with different band gap energies. The electrical properties will be dependent on the alignment of the energy bands from the two structures. The band alignment of the heterojunction can be divided into three types, the straddling gap (type I), the staggered (type II), and the broken gap (type III) as schematically shown in figure 1.2.[4]

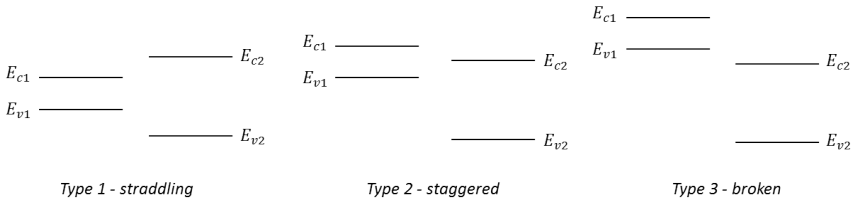

Figure 1.2: Different types of band gaps configurations in heterojunctions.

An important material group for this is the combination of III-V semiconductors. III-V semiconductors are composed of atoms from group III and V of the periodic table and can form binaries, ternaries and quaternaries. The band gap for the alloy depends on the percentage of the constituting elements, as well as the structure. Therefore, we can modulate the band gap alignment of heterojunctions between two III-V semiconductors by engineering the elemental content and crystal structure at will.

1.1.2 Semiconductor devices

Semiconductors can be used for several devices such as solar cells, diodes and transistors. Nanowires of InAs-GaSb with axial or radial heterojunctions, may be employed as electronic components e.g. different types of diodes and field effect transistors (FETs). Nanowires can be synthesized in a large variation of 1D homo- and heterostructures (Fig. 1.1) to engineer the properties. In addition their smaller size opens up the field for smaller and more efficient devices. The III-V material system investigated in this thesis has a potential application as FETs which are described briefly.

A FET is an electronic device that is widely used in integrated circuits. It is made of a semiconductor material, which conductivity can be altered by external forces. An inversion channel, i.e. where the opposite charge carriers are accumulated, can be created by inducing an electrical field in the area. The electrical field is created by applying a *gate voltage*. The current through this area between the *drain* and *source*, can be determined by the *gate voltage*. A simple schematic of a p-substrate based FET is illustrated in figure 1.3.[5]. In the recent years heterostructured nanowires have shown to be promising as nano-sized FETs and even tunneling FETs (TFETs). These heterostructured nanowires can be synthesized by a bottom-up technique called epitaxy, which will be discussed in the next section.

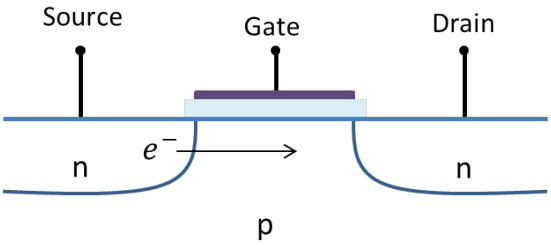

Figure 1.3: A simplified schematic of a FET where n and p denoted the regions where electrons and holes are the charge carriers respectively. By applying a voltage to the gate an accumulation of electrons can be created near the gate and the electrons can go from the source to the drain.

1.1.3 Nanowires and the growth mechanism

Nanowires (Fig. 1.1) can be synthesized by epitaxial growth in a controlled environment. Epitaxy is a common bottom-up approach in which the atoms self-assemble and "grow" up from a substrate to form the 1D structure of a nanowire. One of the common techniques is

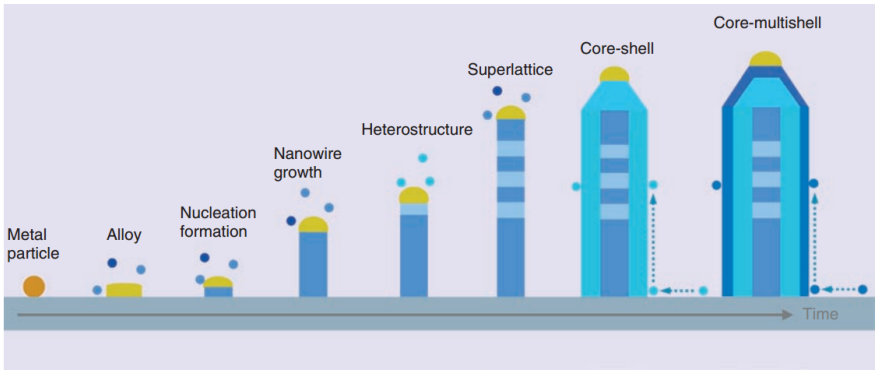

Figure 1.4: A simplified schematic of the epitaxial growth process of a nanowire, heterostructure, superlattice, core-shell and core-multishell. The structures until the superlattice is seen to form by incorporation of growth species in the seed particle by the VLS mechanism. The shells of the core-shell structures are instead seen grow by the VS mechanism and diffusion from the substrate. An axial growth due to VLS mechanism is seen in the core-shell structures. The figure is adapted from ref. [1]

metal-organic vapor phase epitaxy (MOVPE) in which the nanowires can grow either from a template, seed-particle assisted, or be self-seeded.

In the case of seed-particle assisted growth, the seed particles are deposited on a substrate and the substrate is placed in the MOVPE reactor (we can also have in-situ seed particles). The precursors with the desired elements are injected into the reactor in order to create the right gaseous environment. Additionally, the temperature is controlled to achieve the desired structure of the manufactured nanowire. Seeded nanowires are mostly grown by the vapor-liquid-solid (VLS) mechanism as the precursor atoms in gas phase are incorporated in the melted seed particle and accumulate until it reaches supersaturation. The precursor species start to deplete from the seed particle and assemblies in the interface of the liquid seed particle and the solid substrate. The growth is (ideally) only axial and the growth takes place at the interface of the liquid seed particle and the solid nanowire. By changing precursor or other growth conditions during growth, axial segments of different structures (or materials) can be achieved in the same nanowire. An illustration of the MOVPE process is shown in figure 1.4. [6]

Radial overgrowth, so called tapering (Fig. 1.1b), can occur during the axial growth. This is due to the accumulation of atoms on the substrate which diffuse up from the base of the nanowire and create a shell by the vapor-solid (VS) growth mechanism [7]. At lower growth temperatures, where the diffusion flux is lower, tapering effects have also been found due to sidewall nucleation [8].

Core-shell structures can be acquired by first growing a nanowire as described, which will act as a substrate for the shell. This nanowire is called the core, and after it has been grown the initial growth run is terminated. A new growth run, with other growth conditions, will be initiated without removing the nanowires from the MOVPE reactor in order to acquire a shell. The shell growth will take place along the side walls due to the VS mechanism. However, axial growth at the interface between the seed particle and nanowire can occur as well due to the VLS mechanism, see figure 1.4.

The VS mechanisms is a layer-by-layer mechanism called Frank-Van der Merve growth mode where the adatoms attach to a flat substrate to form atomically flat islands that expands into layers. If the substrate is composed of a surface with terraces and steps, the growth can occur by a step-flow mechanism where the adatoms attach to the steps.[6]. Under the right conditions radial growth will occur evenly over the nanowire core.

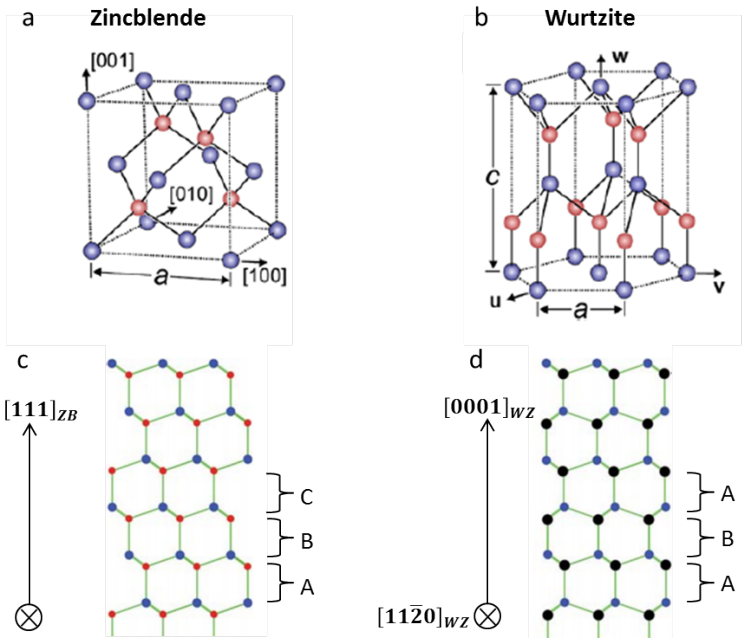

Figure 1.5: The crystal unit cell for (a) ZB and (b) WZ. The red atoms are seen to fill four of the eight tetrahedral sites of ZB and half of the tetrahedral sites in the WZ unit cell. The stacking order of the (c) ZB and (d) WZ in the growth direction is illustrated. (a-b)[6] (c-d)[9]

1.1.4 Crystal structures and physical properties

In crystalline materials atoms self-arrange in the most energetically favorable crystal structure under the present environment. During epitaxial nanowire growth the structure and composition can be controlled by the growth conditions which might differ from bulk. The atomic arrangement is described with the smallest repeatable unit, i.e. the unit cell. The common crystal structures for III-V compounds are the cubic zincblende (ZB) and the hexagonal wurtzite (WZ) structures. Since the atomic arrangement is different in different crystal structures, stoichiometric alloys can have different properties depending on the crystal structure. The crystal structure of nanostructures can be engineered, under the right conditions with more freedom compared to bulk materials.

The ZB structure can be thought of as a face centered cubic (FCC) unit cell of one atom species with the other atom species filling four of the eight tetrahedral sites (Fig. 1.5a). The WZ structure is built up by a hexagonal unit cell. One atom species form the hexagonal closed packed (HCP) structure and the other atom species occupies half of the tetrahedral sites (Fig. 1.5b). The growth directions are [111] and [0001] for ZB and WZ, respectively. The stacking sequence, along the growth direction, for the bilayers of ZB is ...ABCABC... and for WZ ...ABAB... Each bilayer contain one atomic layer of each element (Fig. 1.5c, d). The atomic structure of ZB and WZ are compared in figure 1.6 and helps to understand the differences between the two.

1.1.4.1 Structural issues

Structural defects are the structural artefacts which deviate from the pure crystal structure. *Stacking faults* occur when the stacking order for a crystal structure is disrupted. Stacking faults may change the band alignment and hence the electronic properties of the material. A common stacking fault is *twinning* which occurs when the stacking order is mirrored, for example ...ABCACBA... in ZB where A is called the twin plane. A *twin-plane superlattice* (TPS) is created by repeated twin planes with a number of layers in stacking order in between. TPS segments can be grown with a high degree of control [11]. These kinds of structure

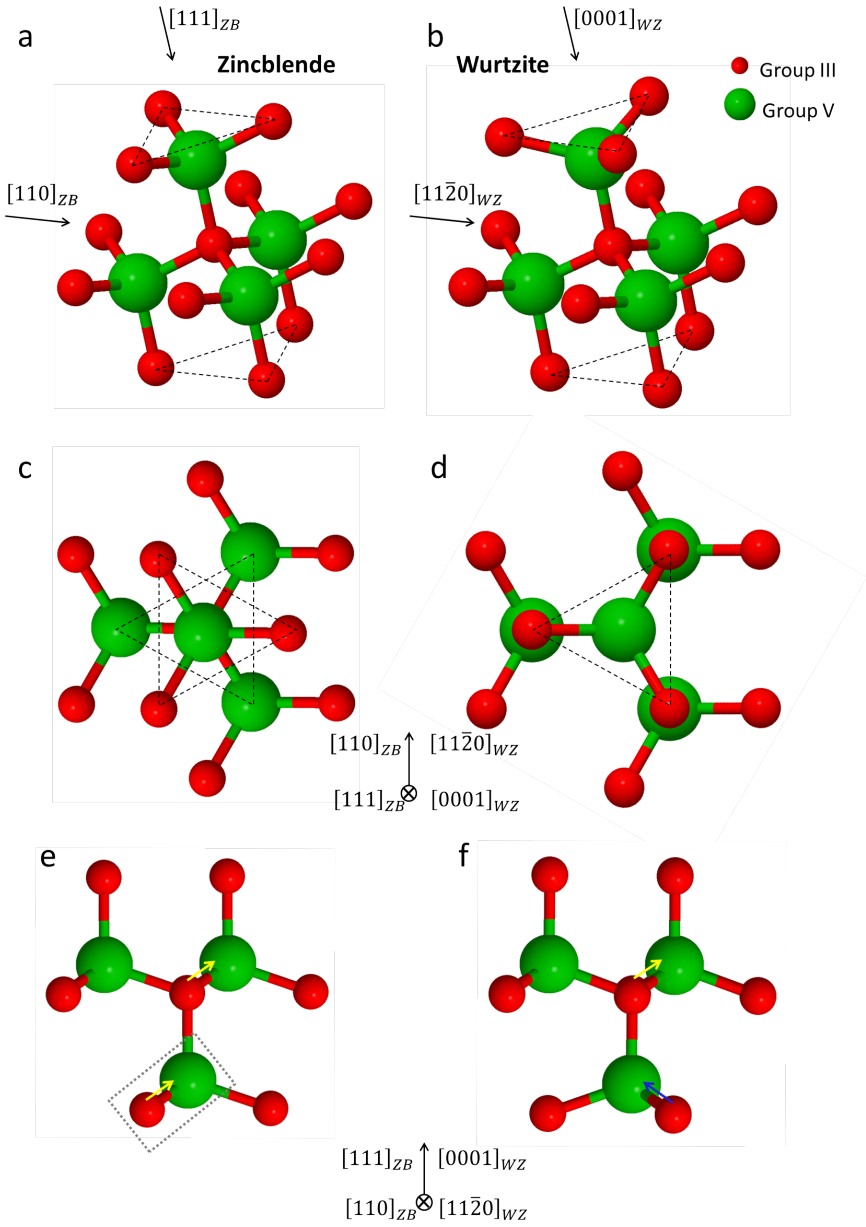

Figure 1.6: The structure of ZB and WZ from different viewing angles [10]. The group III atoms are illustrated by the red (smaller) atoms and the green represents the group V atoms. Two black triangles are marked in (a) ZB, (b) WZ, and the alignment of those seen from the top view of (c) ZB and (d) WZ. The models are aligned to zone axis of $< 110 >$ and $< 11\bar{2}0 >$ for (e) ZB and (f) WZ and the direction of the dumbbells are indicated with arrows. One of the dumbbell units in (e) is indicated with a dashed rectangle. The arrows have the same direction in ZB (yellow), for WZ however the direction changes between the layers (blue and yellow).

variations can be achieved intentionally during formation of the nanostructures, but can also as occur unintentionally during the growth process.

1.1.4.2 Polarity

In crystal structures such as WZ and ZB where the structure can be composed by different elements, the charge transfer between them will result in atomic pairs (dumbbells) of opposite charge. The chemical bond in these atomic pairs will hence have a partial ionicity. This is known as polarity and implies that the crystal has an internal electrical field. This is known to impact physical properties such as the electronic structure and local charge carrier distribution. [12]. The polarity of III-V ZB compounds lie in the $< 111 >$ directions [13] and the polar axis of WZ is $< 0001 >$ [14]. The direction of the dumbbells can be seen from zone axes $< 110 >_{ZB}$ and $< 11\bar{2}0 >_{WZ}$ and are illustrated in figure 1.6(e, f), where the dumbbell directions are indicated with arrows. The polar axes of the ZB and WZ are also the common growth directions of these structures. The polarity can be determined by atomic resolution STEM images where the atomic dumbbells are distinguishable. The knowledge about the chemical composition together with the z-contrast experimental data can be used to conclude the atomic ordering and hence the polarity [12]. This will be described further in the next chapter. The polarity is said to be cation (/anion)-polar if the group III (/V) element is on top in the growth direction.

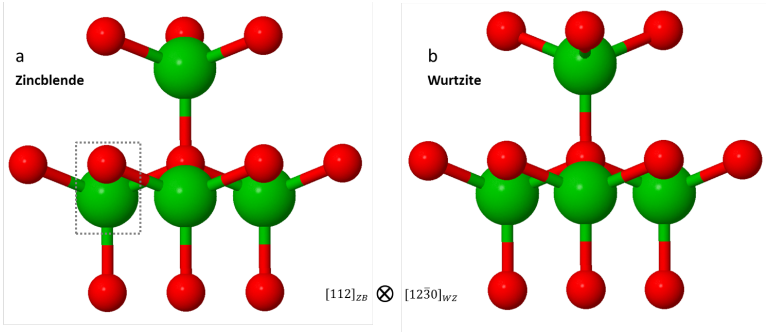

Figure 1.7: The atomic model for (a) ZB and (b) WZ on zone axis $[112]_{ZB}/[12\bar{3}0]_{WZ}$. One of the dumbbell units in (a) is indicated with a dashed rectangle. The crystal structure of the material cannot be distinguished, in comparison to the viewing angle in figure 1.6(e-f).

1.1.4.3 Core-shell interface

To observe the crystal structures by HRTEM (section 2.3.2) the samples must be oriented to a proper zone axis. This is when the atomic columns lie parallel to the viewing angle. The zone axes where the crystal structures can easily be seen are $< 112 >$ and $< 110 >$ for ZB, which are equivalent directions for $< 12\bar{3}0 >$ and $< 11\bar{2}0 >$ WZ, respectively. The important difference between these two zone axes is that from $< 112 >_{ZB}/< 12\bar{3}0 >_{WZ}$, as seen in figure 1.7, ZB and WZ structures cannot be distinguished, because the direction of the dumbbells and consequently the stacking sequences are not distinguishable. Moreover, the dumbbells are vertically aligned, therefore the distance between the cation and the anion in each dumbbell unit is less. The distance between the anion and cation is 0.15 nm and 0.09 nm for $< 110 >_{ZB}/< 11\bar{2}0 >_{WZ}$ and $< 112 >_{ZB}/< 12\bar{3}0 >_{WZ}$ respectively. This can cause problems, because we will need higher spatial resolutions in order to resolve the dumbbells oriented on zone axis $< 112 >_{ZB}/< 12\bar{3}0 >_{WZ}$ than $< 110 >_{ZB}/< 11\bar{2}0 >_{WZ}$, and hence determine the polarity. The polarity is determined by using scanning TEM (STEM) in which we have a z-contrast (section 2.2.4). The details on how to determine the polarity by this method will be discussed in chapter 4.

On the one hand, we need an appropriate zone axis to resolve the crystal structure and the

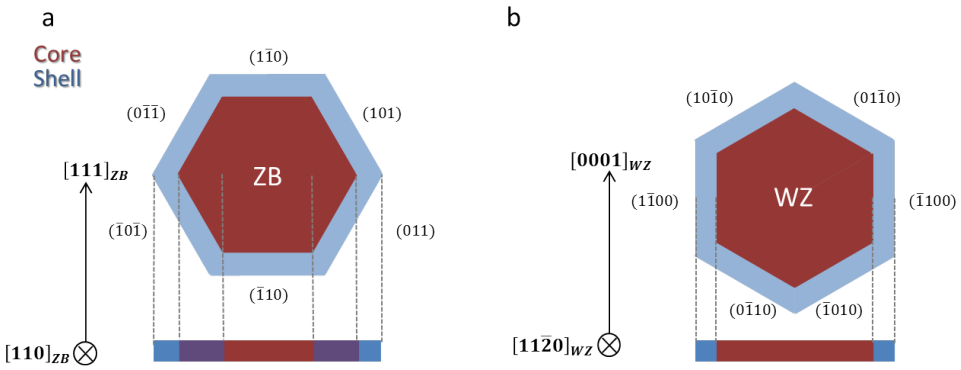

Figure 1.8: A schematic of the interface in a cross-section of a core-shell nanowire structure. The red and blue bar underneath the cross-sections represent the contrast from each structure in the resulting TEM image. The purple area visualize how the core-shell interface on zone axis $[110]_{ZB}/[11\bar{2}0]_{WZ}$ is a mixture of the two structures for ZB but clear for WZ.

polarity. On the other hand, study of the heterointerfaces is crucial. Semiconductor nanowires mostly have hexagonal cross-sections with six lateral facets which will be aligned along one of the mentioned zone axes. Having the lateral facets aligned is an important advantage, because it facilitates the study of the radial heterointerfaces of the core-shell nanowires. In the case of our material, the common lateral facets are {011} for ZB and $\{1\bar{1}00\}$ for WZ. The interfaces of a core-shell structures can only be seen in $< 112 >_{ZB}$ and $< 11\bar{2}0 >_{WZ}$, as illustrated in figure 1.8, because otherwise we will have an overlapping region between the core and the shell. However the polarity is also an interesting property of the material to be determined. The polarity of the ZB and WZ structure can be seen in figure 1.6(e, f), which are on zone axis $< 110 >_{ZB}$ and $< 11\bar{2}0 >_{WZ}$ respectively. However, it cannot be resolved from $< 112 >_{ZB}/< 12\bar{3}0 >_{WZ}$ zone axes as can be seen in figure 1.7. Due to this, fortunately, the polarity as well as a good interface contrast can be achieved for our WZ structures simultaneously. This is not the case for ZB where only one can be observed at a time.

1.1.5 Growth of lattice-mismatched heterostructures

Epitaxial growth methods such as MOVPE can be used to grow layered heterostructures, superlattices and core-shell nanowires. A so called lattice-mismatch between the layers is present if the constituting compounds have different crystal structures, or different dimensions of the unit cells (lattice parameters). This mismatch will lead to strain or deformation at the interface in order for the overlaying structure to adapt the underlying structure.

A heterostructure of two materials with the same crystal structure can still have different lattice parameters depending on the constituting atoms. As an example, the (0001) plane distance of GaSb WZ is 6.923 Å and for InAs WZ 6.844 Å. The lattice mismatch, f, of the two binaries can be calculated with the lattice constants for the binary acting as substrate a_s and the layer a_L on top:

$$F = \frac{a_s - a_L}{a_L}. \tag{1.1}$$

The percentage lattice mismatch between an InAs substrate and a GaSb layer are hence about 1.15%. In order for the overlaying structure to adapt to the substrate it need to compensate the lattice-mismatch, either elastically or plastically. Elastic relaxations occur if the structure can be laterally relaxed and no dislocation will be induced, as seen in figure 1.9(a,b). However this is only achievable until the layered structure reach a threshold strain. To compensate the lattice-mismatch after the threshold strain, a plastic relaxation occurs. A plastic relaxation is a

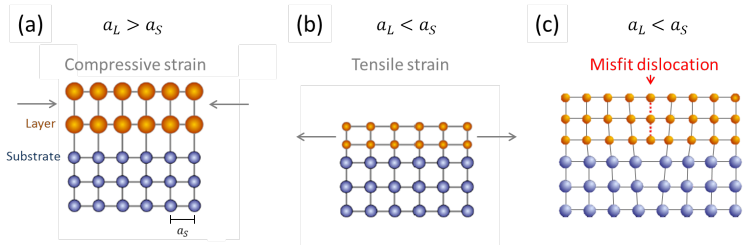

Figure 1.9: The figure illustrate the (a-b) elastic and (c) plastic relaxation that can occur during growth of lattice-mismatched heterostructures. The lattice constant of the substrate, a_s is indicated in (a). In (a) the unstrained lattice constant a_L is larger than a_s and the layer is compressively strained. In (b) the unstrained lattice constant, a_L, is smaller than the a_s and hence tensely strained. In (c) the lattice mismatch has been compensated by a misfit dislocation of the layered structure.

dislocation of the crystal structure to compensate for the strain induced by the lattice mismatch and depends on the elastic energy at the interface. A common type of misfit dislocation is an inset of an extra atomic layer, illustrated in figure 1.9(c). [6]. This threshold is higher in nanowires as strain in one direction can be relaxed from the other direction. Therefore, it is less likely to have misfit dislocations when the lattice mismatch is low.

1.2 The InAs-GaSb system

InAs and GaSb are narrow-bandgap semiconductors that have a high electron (n-type) and hole (p-type) mobilities, respectively, which makes them interesting for electronic devices [15]. The broken band gap give rise to interesting charge transport phenomena [16]. InAs-GaSb ZB systems have previously been investigated in detail, in bulk [16], as 1D axial heterojunctions [17][18][19], core-shell structures [15][20] and selective core-shell structures [21]. However, the growth of WZ GaSb nanowires has not been achieved, only short segments of WZ have been grown axially on nanowire templates [22]. Also the band structures for the different III-V crystal structures have been found to differ. Therefore, it is interesting to investigate GaSb in WZ structure. In contrast, InAs nanowires is a well-known material and the structure can be engineered with a high degree of control [23].

The lattice mismatch of the two WZ binaries in the [0001] direction is 1.15 % which indicates that a core-shell structure could be grown with small strains at the interface. An InAs-GaSb WZ core-shell structure is of interest to synthesize in order to characterize the structure and investigate its electrical properties. In addition is it of interest to determine if it is possible to grow GaSb as a WZ shell and the well-known InAs is considered suitable template due to the small lattice-mismatch.

Research of nanowires with axial heterojunctions of ZB InAs-GaSb has been reported [18][17]. The large difference in the electron affinities of antimonides and arsenides result in that the top valence band of GaSb lies above the conduction band of InAs creating a broken band gap heterojunction [24][25][26]. It is this band structure which is of interest in order to construct a TFET. The TFETs are similar to the FET, but instead it use quantum tunneling as the switching mechanism. This result in that a lower gate voltage is needed to achieve a higher drain current. Hence, the TFETs have the possibility to decrease the power dissipation in integrated circuits which would enable more efficient electrical components. [27].

Research of radial heterojunction of ZB InAs-GaSb nanowires have found that the semiconductor properties differ depending on the core-shell morphology [15][28]. Even small differences, as a few nm differences in the shell thickness as well as the core-shell ratio have been observed to change the electrical properties dramatically [15]. Consequently, structural characterization of such nanowires is of interest in order to understand from where the variety of electrical properties originates.

1.3 Transmission electron microscopy

For the development of these electronic components, the structure needs to be characterized in order to understand how it affects the device performance. To be able to conduct structural analysis at an atomic scale, a diversified instrument or a combination of many is needed.

One instrument that stands out for the characterization of nanostructured materials is transmission electron microscope (TEM). TEM, and electron microscopy in general, is superior in resolution and magnification compared to the conventional visible light microscope (VLM). The electrons used in TEM are accelerated in order to have a higher energy than light, and hence a shorter wavelength. This is one of the features which makes it possible to achieve a higher resolution with a TEM. The electron-matter interaction in the specimen can in addition be used to extract a lot of information about the material by means of a large variety of techniques. For example elastic scattering is used in imaging modes such as conventional TEM, scanning TEM (STEM), and high resolution TEM (HRTEM) to resolve the morphology and structure of the specimen. On the other hand, compositional information is given by inelastic electron-matter interactions which are used for energy dispersive X-ray spectroscopy (EDX) and electron energy-loss spectroscopy (EELS). In the following some other commonly-used techniques are mentioned for comparison.

Atomic force microscopy (AFM) and scanning tunneling microscope (STM) use a small tip rastering over the materials surface and respectively measure the atomic force or the tunneling current. AFM can be employed to gain topological information. STM probes the electron density of states of the surface atoms. With these methods it is possible to observe the properties of the surface in atomic resolution. However, for a material that is interesting for its layered structure, or inside, a cross section analysis would be required. Such analysis is time consuming and needs a lot of difficult preparation steps and only gives surface information of that particular cross-section.

X-ray diffraction (XRD) is another common technique which can be used to determine the crystal structure of crystalline materials. In this technique X-rays are directed at the crystal and the scattering due to the crystal lattice planes will create a diffraction pattern. The diffraction pattern is based on the crystal lattice structure and can be achieved from the TEM as well with electron beams. However, one difference is the illumination source, where X-rays are less energetic than the electrons used in TEM and the risk for beam damage hence decreases. Hence does XRD have a low spatial resolution which makes it difficult to observe small structural changes. [29]. TEM has a high spatial resolution and in addition can the crystal structures be determined by diffraction as well as imaging. It is easy to switch between imaging and diffraction mode which enables correalating the positional information to the diffraction pattern. It is worth mentioning that XRD with a synchrotron light source can generate information with high spatial resolution. However, the difference in availability and cost for the two instruments is rather immense. The approximate cost of building the electron accelerator facility MAX IV laboratory was SEK 6 billion [30] while a state-of the-art TEM can be bought for approximately SEK 50 million [31]. Another disadvantage that should not be disregarded is the difference in space and staff requirements for the two methods.

The TEM with its additional detectors is superior in spatial resolution. Moreover, it offers an ample range of techniques each of which can provide crucial information about the morphology, crystal structure, chemical composition, and even optical and electronic properties of the material. On the other hand the instruments are not extremely expensive or difficult to handle, and they are available in many labs. In addition, recent technology advancements have improved their stability and reliability of the acquired data. In the next chapter we will discuss the details of the TEM methodology.

Chapter 2

Methodology

In this work transmission electron microscopy was used in order to investigate the physical structure and chemical composition of the InAs-GaSb nanowire samples. The transmission electron microscope (TEM) utilizes electrons as the illumination source and detects the transmitted electrons to form an image. Secondary signals as characteristic X-rays which are generated from inelastic electron-matter interactions can be detected in order to obtain elemental information. The TEM have a high spatial resolution and can be used to image features of a few nanometers or less. This chapter describes important concepts of TEM analysis as well as different TEM techniques employed to carry out the structural analysis of the InAs-GaSb system.

2.1 The transmission electron microscope

The TEM (Fig. 2.1 can be divided into three larger sections, each with different functions; the illumination system, the objective lenses with the sample stage, and the imaging system. To achieve a high spatial resolution it is of importance that every part in the TEM setup is optimized and aligned properly, as many parts are interdependent and a small error can accumulate or be difficult to correct sufficiently further down the optic axis. The entire instrument operates under high vacuum as the electrons interact with materia. The different sections of the instrument will now be describe top-down.

2.1.1 The illumination system

The pre-specimen part of the instrument column is called the illumination system and it is here that the incident electrons are generated, accelerated and directed along the optic axis on to the specimen. The electrons are generated by an electron gun and accelerated to a certain voltage. Two common types of electron guns are thermionic guns and field emission guns (FEG). The former generates electrons by applying heat to a small filament until it emits electrons. The FEG instead applies an electrical field to the filament until it emits electrons. A Schottky FEG is heated in addition to the applied electrical field whereas a cold FEG operates at ambient pressure.

In order to achieve a high spatial resolution some properties of the high-energy electrons are important. Among those are firstly the electron energy which is determined by the acceleration voltage. This is important as it affects the resolution of the analysis (section 2.2.2). Moreover, the energy spread is also an important parameter, which should be as small as possible to avoid chromatic aberrations (section 2.2.3). In comparison to the thermionic electron gun the FEG emits electrons with a smaller energy range. The former operates by supplying enough thermal energy for the electrons to overcome the work function barrier while the latter applies

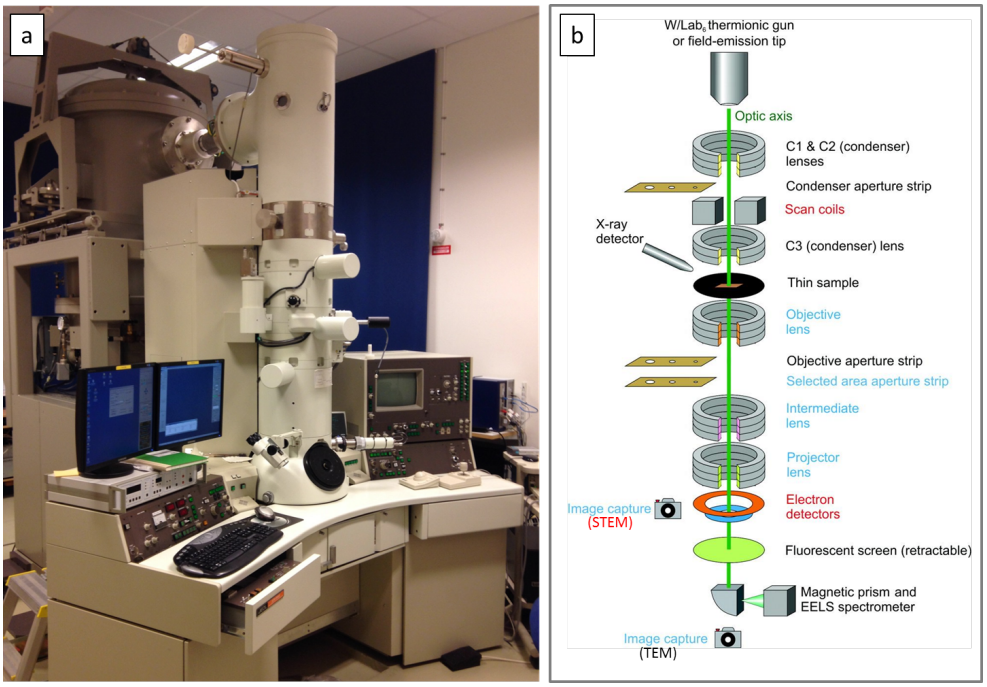

Figure 2.1: (a) The JEOL 3000F TEM. (b) A schematic of the interior of the TEM column, adapted from [32].

the electrical field to lower the work function barrier so the electrons can tunnel out of the tip. The electrons are accelerated to a certain voltage, usually as high as the microscope allows, in order to achieve the highest possible spatial resolution. After the accelerator a number of condenser lenses and apertures are located, with the purpose of condensing and spreading the beam in the desired manner, see figure 2.2.[33]. The lenses are composed of circular electromagnetic coils and the current can be changed to alter the strength of the magnetic field, $\boldsymbol{B}$, which is the electron-focusing strength of the lenses. The Lorenz force, $\boldsymbol{F}$, on the electrons (with the charge -e) that travels with velocity $\boldsymbol{v}$ in this magnetic field is given by the equation

$$\boldsymbol{F} = -e(\boldsymbol{E} + \boldsymbol{v} \times \boldsymbol{B}), \tag{2.1}$$

where the electrostatic field, $\boldsymbol{E}$, is assumed to be zero for purely magnetic lenses. This leaves the expression

$$\boldsymbol{F} = -e(\boldsymbol{v} \times \boldsymbol{B}). \tag{2.2}$$

The vector cross product means that if the electrons pass through the middle of the lens (parallel to $\boldsymbol{B}$) the force will be zero, and any velocity component perpendicular to the magnetic field will result in a force on the electron. This force sets the electron off to a circular motion, which in combination with the velocity will create a helical movement that will focus the electron. [34].

A number of condenser apertures are also available in the system to physically limit the electron beam, however, the purpose for this will not be discussed further.

2.1.2 The objective lenses and the sample stage

The objective lenses and sample stage are located after the illumination system, see figure 2.1. In our case, the sample is placed on a copper grid with a thin amorphous lacey carbon film

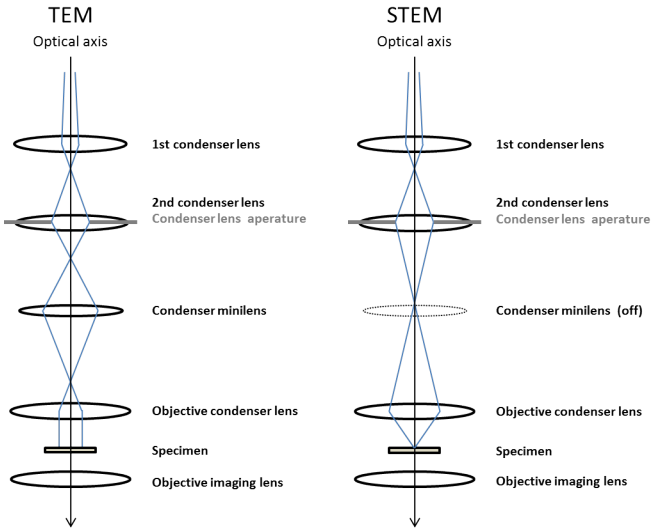

Figure 2.2: The beam ray paths in the illumination system down to the specimen are illustrated for TEM (left) and STEM (right).

and mounted on the specimen holder. The specimen holder is inserted into the TEM so that the specimen is placed at the sample stage in between the objective lenses 'pole pieces'. The height as well as the position and the tilt in one or two directions can usually be adjusted with a goniometer which is the sample stage. The design of the sample holder determines the tilt capacities. The objective condenser lens role is, together with the condenser lenses, to illuminate the specimen in the desired manner which depends on the imaging method used (Fig. 2.2). The objective imaging lens forms an image in the image plane and a diffraction pattern (DP) in the back focal plane (BFP) in the imaging system as seen in figure 2.3 which describes the beam paths in the imaging system. The x-ray detector for EDX analysis is placed in the proximity above the sample.

2.1.3 The imaging system

The imaging system is the post-specimen part of the column and comprises several intermediate lenses and apertures whose main objective is to project the image or DP down to the viewing screen or charge-coupled device (CCD) camera. The employment of the apertures is discussed in section 2.2.4. The image or DP is then projected down, with intermediate lenses, to a fluorescent viewing screen which emits green light as the electrons hits it and a shadow of the sample or its DP can be seen. A CCD is located under the viewing screen and used to acquire the final image or DP. Electron detectors are used for imaging in scanning TEM (STEM) mode and are placed above the viewing screen (Fig. 2.1).

2.2 Concepts

2.2.1 Electron-matter interaction

Incident high-energy electrons can interact with the atoms in the specimen in several different ways. The interactions can either be elastic, where the electrons do not lose energy, or inelastic where the electrons lose kinetic energy during the interaction.

The inelastic interactions occur when the incident electrons have a high enough energy to transfer some of it during the collision with the atoms in the specimen, which leads to a number of different secondary signals. The secondary signals can be seen in figure 2.4. Secondary

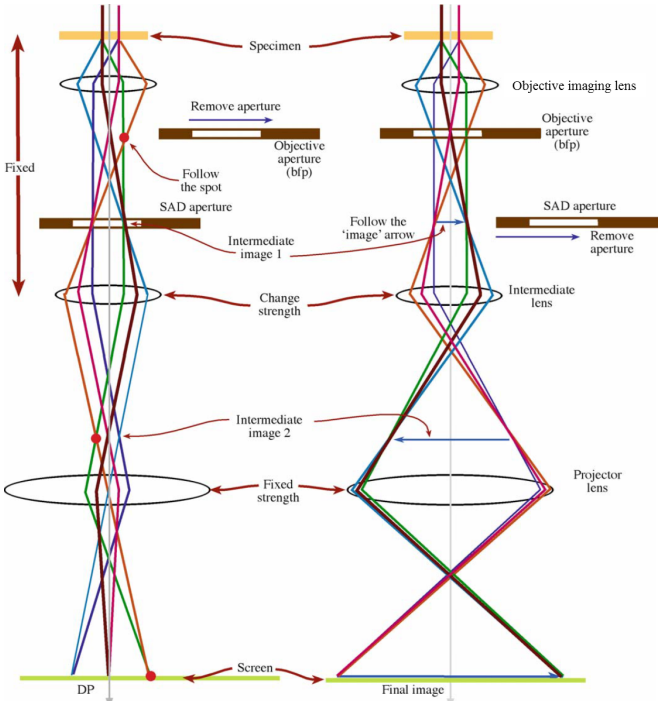

Figure 2.3: The figure illustrates the beam paths in the imaging system for TEM. The left schematic show the beam paths when a DP is desired to be imaged. The right schematic show the beam paths in imaging mode [33].

electrons (SE) and back scattered electrons (BSE) are mainly used in scanning electron microscopes (SEM). The inelastic interactions can cause the emission of characteristic X-rays. These X-rays photons are detected in the spectroscopy technique energy dispersive X-ray spectroscopy (EDX) (section. 2.4.1). The inelastically scattered electrons are utilized in the TEM technique electron energy loss spectroscopy (EELS). Other inelastic scattering events are emission of Auger electrons, visible light emission and Bremsstrahlung X-rays, which are out of the scope of this work. The elastically scattered electrons are used for the imaging methods; conventional TEM, high resolution TEM (HRTEM) and scanning TEM (STEM).

The elastic scattering interactions are due to Coulomb interactions between incident electrons and the nucleus or electron orbitals of the atoms in the specimen. The scattering angle depends on the Coulomb force on the incident electrons and its strength depends on the distance from the nucleus. The elastic scattering events that are used in the TEM techniques described in this thesis can be seen in figure 2.5. The amount of elastically scattered electrons is the main cause for the image contrast (section 2.2.4) in TEM and STEM as well as the formation of diffraction patterns (section 2.2.5).

2.2.2 The concept of resolution

The 'highest spatial resolution' is the smallest distance that a microscope can resolve. The highest resolution of a visible light microscope (VLM) is described by the Rayleigh criterion

$$\delta = \frac{0.61\lambda}{\mu \sin \beta}, \tag{2.3}$$

where λ is the wavelength of the visible light source, μ the refractive index of the viewing medium and β the semi-angle of collection of the viewing lens. By the assumption that $\mu \sin \beta$ is unity, the resolution is 0.61λ and with green light with $\lambda = 500$ nm, theoretically the smallest viewable distances are about 300 nm. In nanotechnology this resolution is not enough since

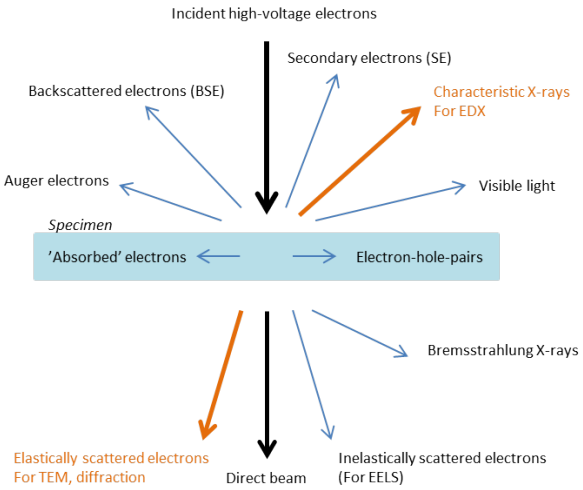

Figure 2.4: The electron-matter interactions in electron microscopy. The signals which are used in TEM and in this thesis are colored in orange, i.e. the elastically scattered electrons and the characteristic x-rays. The figure is adapted from ref. [33]

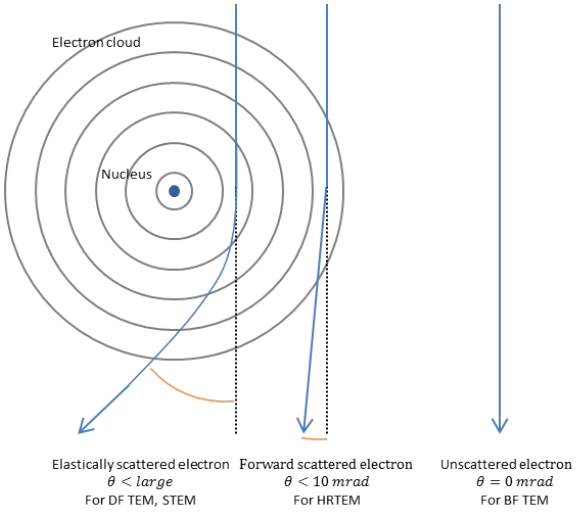

Figure 2.5: Illustration of the elastically scattered electrons. The scattering angle depends on the distance from the nucleus and the different utilization of these variations is noted in the figure. The figure is adapted from ref. [33].

the structures have dimensions of a few 100 nm. Louis de Broglie's equation connects the kinetic energy, E, of the electrons with their wavelength and by ignoring relativistic effects the wavelength, λ, can be calculated by

$$\lambda = \frac{1.22}{\sqrt{E}}, \tag{2.4}$$

where E is in eV and λ in nm. A typical TEM acceleration voltage is 300 keV which gives an electron wavelength of about 0.0023 nm. However, due to the imperfection of the magnetic lenses and electron source in the instrument this is only a theoretical value if these aberrations are not corrected. Nevertheless, by employing Rayleigh's criterion, it is obvious that the resolution will be significantly higher with such small wavelengths than the wavelengths of visible light. [33].

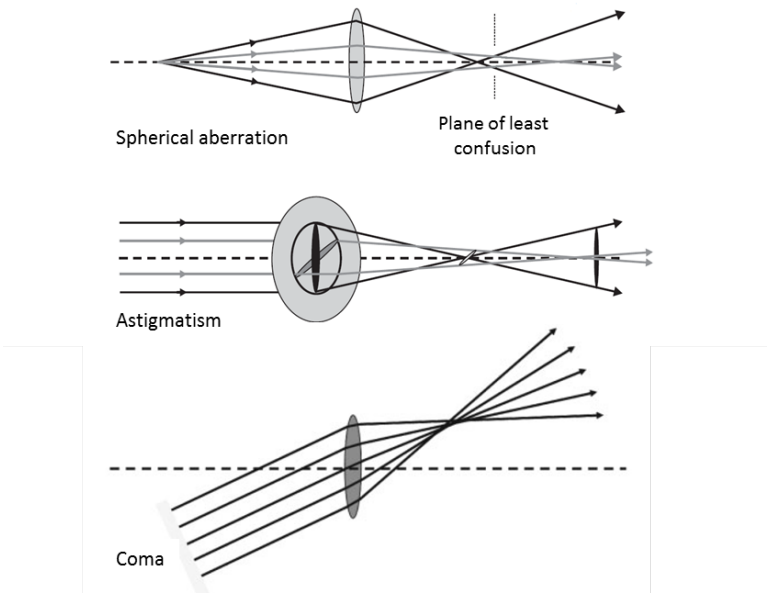

Figure 2.6: The three monochromatic aberrations: spherical aberrations where the on- and off-axis electrons are not focused to the same point, astigmatism when the focused rays are displaced along the optics axis depending on the angle of the beam, and coma where off-axis rays are brought to focus off-axis. The plane of least confusion is the plane where the aberrations have the least distortion effects. The figure is adapted from ref.[34].

2.2.3 Aberrations

Aberrations are the optical distortion effects that are present due the difficulty of creating an ideal optical system. If the system is not ideal the image will not perfectly reproduce every point on the object which limits the possible resolution of the microscope. The aberrations can be divided into two groups depending on the source of the distortion; from anisotropy in the lenses (*monochromatic aberrations*) or from the electron beam (*chromatic aberrations*).

Monochromatic aberrations

The most important monochromatic aberrations are *spherical aberrations*, *astigmatism* and *coma* which are illustrated in figure 2.6. Spherical aberrations originate from the round magnetic lenses as they induce a magnetic field which does not increase linearly with the distance

from the center. As a consequence the force increases too much in comparison to the force needed to focus the off-electrons further from the optic axis compared to the on-axis electrons closer to the center. Hence, the electrons will be focused at different points on the optics axis depending on where it passes through the magnetic field. Astigmatism occurs when the focused rays are displaced along the optic axis depending on the azimuthal angle of the beam. Coma occurs when the slightly off-axis rays are not exactly brought to an off-axis focus point, depending on the distance from the center of the lens (see Fig. 2.6)[34].

Chromatic aberrations

Chromatic aberrations come from the energy spread of the electrons in the electron beam. The energy spread mainly originates from the electron source. The other sources of chromatic aberration are the fluctuations of the acceleration voltage or the energy losses which can occur during elastic electron-matter interaction with the specimen. Due to the energy differences of the electrons, the lenses will affect them differently and they will be brought to focus on different points along the optic axis. Note that anisotropy in the lenses can also contribute to the chromatic aberrations.

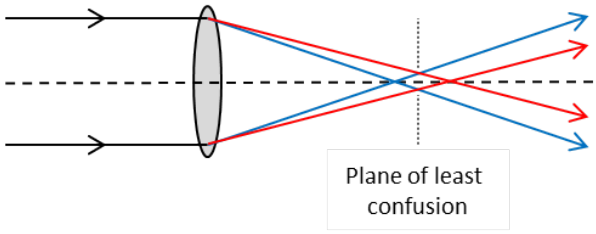

Figure 2.7: The chromatic aberration is illustrated with visible light rays where the higher energy light (blue) is focused more than the lower energy light (red). The plane of least confusion is the plane where the aberrations have the least distortion effects. The figure is adapted from ref.[34].

2.2.4 Contrast

Image contrast is the intensity difference in an image in electron microscopy. Intensity is related to the number of electrons that are detected. Generally the more electrons detected a higher intensity is achieved and hence the image will appear brighter. However the appearance of the images depends on which electrons are detected, as the image contrast in TEM originates from the scattering of the incident electrons by the sample. The electron wave's amplitude and phase can both change during this interaction and both types contribute to the contrast in TEM. As both amplitude and phase changes tend to be present, it is preferable to operate the TEM under conditions where one type of contrast is dominating. This is simply to achieve micrographs that are easier to interpret. In conventional TEM (CTEM), the amplitude contrast is dominating whereas the phase contrast is used in high resolution TEM (HRTEM). The different TEM methods, as CTEM and HRTEM, will be discussed in section 2.3.

Amplitude contrast

The amplitude contrast can be divided into two types, the *mass-thickness contrast* and the *diffraction contrast*. The mass-thickness contrast is due to the fact that electrons will interact more strongly with denser areas, i.e. scatter with a larger angle. In bright field (BF) imaging in CTEM the objective aperture is used to deflect electrons with higher scattering angles in order to image forward scattered electrons. These electrons are scattered at a lower angle or not scattered at all, i.e. they are scattered from the less dense areas of the specimen. This will correspond to the bright areas in the micrograph, and the denser areas will appear darker as fewer electrons from these areas of the specimen are able to contribute to the image. As

the specimens are placed on a specimen holder with holey carbon film the background will be mostly vacuum. Consequently the electrons passing through the background will not be scattered and hence the background will appear the brightest in CTEM imaging.

Diffraction contrast is used by selecting one (or more) of the diffraction spots corresponding to a specific plane. This forms an image with contrast from the electrons interacting only with the atoms in this plane. As the direct beam is entirely excluded the vacuum background will appear completely dark as no electrons from this part are scattered. This imaging technique is called dark field (DF) imaging in CTEM.

Z-contrast

For STEM, DF imaging refers to detecting the electrons that have been scattered with a larger angle (Fig.2.5)(Rutherford scattering), and are collected by a high-angle annular dark-field (HAADF) detector. High resolution mass-thickness contrast is referred to as *z-contrast*, because the contrast depends on the thickness and atomic number (Z) of the material analyzed. In case there is no (or small) variation in thickness, the contrast depends only on the atomic number. In atomic resolution HAADF-STEM imaging this contrast can be used to distinguish the elements, i.e. the heavier atoms appear brighter than the lighter ones Atomic resolution Z-contrast is the contribution of one atomic column at a time which nowadays can be detected by means of aberration corrected microscopes.

BF and DF STEM imaging will be described more thoroughly in section 2.3.3.

Phase contrast

The phase contrast originates from the electron waves in which amplitudes remain unaffected but undergo a phase change. This will result in an image where the atomic columns can be resolved in crystalline materials. The mechanism for the phase contrast is discussed in connection with HRTEM imaging (2.3.2).

2.2.5 Diffraction

Due to the wave-particle duality of the electrons they will not only scatter, but the scattering will cause interference of the waves; which will create a diffraction pattern in the back focal plane after the specimen. This diffraction patterns reveals information about the specimen's periodicity, i.e. the crystallinity. From the diffraction pattern the crystal structure and distances between the atoms of the different planes can be calculated. By describing the electrons as waves, Bragg's law which explains the reflection of waves from planes can be used to explain the diffraction from the atomic planes. If the 'reflecting' atomic planes are spaced with a distance d apart and the incident plane wave with wavelength of λ are reflected at an angle θ the total path difference is $2d\sin\theta$ and Bragg's law can be written

$$n\lambda = 2d\sin\theta, \tag{2.5}$$

where n is the order of the diffraction spot from the center. The atomic distance, d_{hkl} , is in reciprocal space $\frac{1}{g_{hkl}}$ where g_{hkl} is the reciprocal lattice vector. The atomic distance between planes can therefore be calculated by measuring the distances between the intensity dots in the diffraction pattern, representing the different planes.[33]

2.3 Methods

2.3.1 Conventional TEM (CTEM)

Conventional TEM (CTEM) is a wide-beam technique used to obtain images at low magnifications, high resolution TEM micrographs and DPs. For CTEM imaging, the electrons in the incident beam are made coherent and parallel by the condenser lenses and broad enough to be projected onto the area which will be imaged as can be seen in figure 2.2(a). The electrons pass through the sample and the image or DP is projected down to the screen/detector by the lenses and apertures in the image forming system. The electron trajectory for imaging and DP in the illumination system can be seen in figure 2.2. We employ CTEM to achieve overview of the samples and a low magnification TEM BF micrograph as presented in figure 2.8(a). The amplitude contrast in BF imaging is mostly the mass-thickness contrast which can be seen in the figure as the nanowires have a darker appearance than the vacuum background. To detect the crystal structure of an area the DP can be imaged (Fig. 2.8(b)). Imaging in DF mode can be employed when the crystal structure is of desire to resolve over a larger area. Dark field (DF) imaging is when a diffraction spot of the DP is filtered by inserting a small objective aperture and the corresponding image will only have the contrast from the selected electrons.

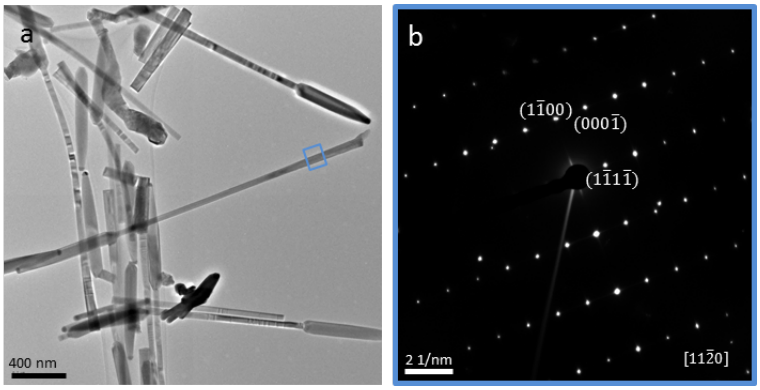

Figure 2.8: (a) A low magnification TEM image of a number of nanowires, the grey background is the vacuum. (b) The diffraction pattern taken from the area marked in blue in (a) is presented with some of the planes indicated.

2.3.2 High resolution TEM (HRTEM)

High resolution transmission electron microscopy (HRTEM) is a powerful technique for imaging crystalline structures with higher spatial resolution than the low magnification TEM imaging in the same microscope. If the specimen can be aligned to a zone axis the atomic columns of the (single-) crystalline structure can be imaged. HRTEM uses of the forward scattered (electrons that are elastically scattered $<$10 mrad) and unscattered electrons, as well as the small energy dispersion of the incident electrons.

In HRTEM we assume that the amplitude of the electrons is unchanged. With this assumption the contrast in the image will not be dominated by the amplitude change of the electrons unlike in low magnification TEM. This requires that the incident electrons have a small energy spread and the specimen is either "one interaction per electron" thin, or single crystalline on zone axis. The electrons are still scattered but it is the phase change that is responsible for the small scattering angles.

As the incident electrons pass through the sample this weak elastic scattering is caused by the interaction with the potential of the atoms. If an incident electron penetrates in the atom's electron cloud, it will be affected by the atom's positive charge of the nucleus. This attractive

force will accelerate the electron before deaccelerating as it moves from the nucleus. There is no energy difference, but an electron affected by the positive potential will go through a phase shift. The phase shift is relative to the distance from the nucleus that the electron has passed (see Fig. 2.5). Meanwhile the electrons passing by the atoms without penetrating the electron clouds, hence moving in between the atomic columns, will not be affected by the positive potential. This is the unscattered reference to the electrons with phase change, and that is the phase difference which gives rise to the contrast in a HRTEM image. Hence will the resulting image will have a contrast between the areas of where the electrons have interacted with the specimen and where it has not. This phenomenon of phase shift occurs in low magnification TEM mode as well but under those conditions the amplitude change is dominant. Amplitude contrast is present in HRTEM as well, but the conditions are chosen in order to let the phase dominate.[33]

The limits of the highest spatial resolution depend on some parameters of the microscope, the microscopes spherical aberration, the wavelength of the incident electrons and the defocus. A certain value of defocus can be calculated in order to obtain the highest possible resolution for each individual microscope, this is the Scherzer defocus. This defocus should be maintained during HRTEM imaging in order to achieve comprehensible micrographs. The mathematics behind the HRTEM technique are found in appendix A.

2.3.3 Scanning TEM (STEM) imaging

In CTEM, described in section 2.3.1, the electrons which form the beam are made coherent and parallel by the condenser lenses in order to illuminate the whole area of interest. The objective lenses then focus the beams in order to project down an image or diffraction pattern. In STEM, however, the condenser lenses are operated to focus the electron beam into a convergent probe (Fig. 2.2) which only illuminates a small part of the specimen, preferably corresponding to one pixel in the micrograph, at a time. Magnetic coils are used to move the probe over the area of interest, one point at a time, while keeping the probe direction fixed (scanning). Due to the smaller illumination area for STEM in comparison with TEM, a higher density of incident electrons is achieved which give rise to a stronger electron-matter signal.

Both BF and DF imaging can be performed in the STEM. As described in section 2.2.4, BF imaging is achieved by imaging the direct beam while DF is formed by excluding the direct beam. In STEM mode electron detectors are placed in and around the beam to detect and image directly without involving the rest of the imaging system . The electron detectors are illustrated in figure 2.9. To acquire BF imaging a bright field detector can be used which only images the electrons from the direct beam. The corresponding method in CTEM is an aperture which is employed to filter the direct beam down to the detector. DF imaging is performed by the same principle, this time by inserting an annular detector around the direct beam. An annular ring which collects electrons of smaller scattering angles is used in annular dark field (ADF) imaging. The technique mostly used in STEM mode in this thesis is high angle annular DF (HAADF) imaging. The high angle annular refers to the appearance of the detector, which is an annular ring that detects the electrons that are scattered from the specimen with a high angle. [33]

2.3.4 Aberration corrected TEM and STEM

As mention before, aberrations in the TEM limit the resolution. A great effort have been taken to correct the spherical aberrations which are induced by the magnetic lenses [34].

In round magnetic lenses, the focusing force rises too strong along the lateral axis and electrons with a larger angle to the optic axis will be focused too much (Fig. 2.6(a)). To overcome these distortions a new set of lenses are introduced, in addition to the round lenses which create a magnetic field parallel to the electrons beam. These are the so called multipole lenses with its magnetic field perpendicular to the electron beam.

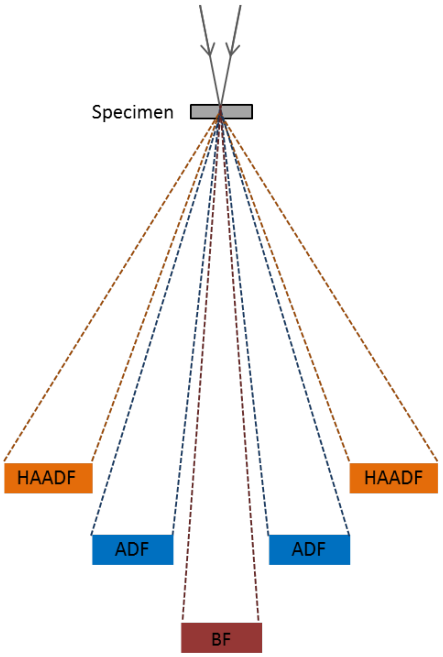

Figure 2.9: A cross-sectional illustration of the annular electron detectors used for STEM imaging .

Multipoles are comprised of smaller units arranged around the beam with alternating poles. The multipoles come in set of a series with 2, 4, 6, 8 poles (dipole, quadrupole, sextupole and octupole, respectively) where all of them change the beam differently. The spherical aberrations cannot be corrected in a single plane but need to be built up in several planes, hence the series of poles are used [34]. The basic idea of the spherical aberration correctors is that the multipole lenses can create negative spherical aberrations which cancel out the round positive spherical aberration of the magnetic lenses [35].

The spherical aberration correctors can be employed either post-specimen in the imaging system as an image corrector or pre-specimen as a probe corrector. In aberration corrected STEM the probe-correctors are used to create a probe with less spherical aberrations. In TEM mode image correctors are employed to create an image with less aberrations.

2.4 Spectroscopy

2.4.1 Energy dispersive X-ray spectroscopy (EDX)

A TEM can also be used for spectroscopy. The methods described so far have not been able to achieve any elemental information; in best case it gives relative information about the constituting atoms atomic number (section 2.2.4). However, as mentioned the incident electrons may cause inelastic scattering events. These event can generate elemental specific X-rays (section 2.2.1). Energy dispersive X-ray spectroscopy (EDX) is a spectroscopy technique based on these scattering events which causes the atoms to emit elemental specific x-rays. The mechanism is visualized in figure 2.10. The incident high-energetic electrons (300keV) are capable of ionizing atoms in the specimen by removing an inner shell electron from it. The ejected electron leaves a hole which leaves the atom in an inner shell ionized state. To compensate this, an electron from an outer shell with higher energy can relax and fill the hole in the lower energy shell so the atom can return to its ground state. For this relaxation event to be possible the electron must adapt the lower energy of the shell. This in done by the emission of a photon with the same energy as the energy difference between the two shells. This energy difference is specific for each elemental atoms' allowed transitions, which makes

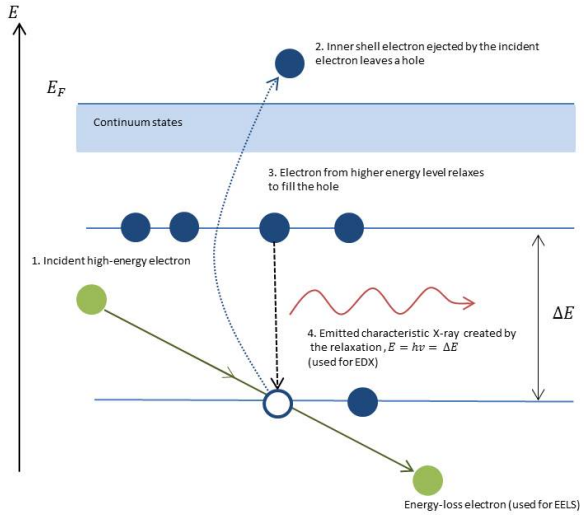

Figure 2.10: The inelastic scattering events used for spectroscopy techniques, EDX and EELS. First an incident high-energy electron ejects an inner shell electron and loses energy, (the energy-loss electron), and leaves a hole in the inner shell. An outer shell electron relaxes to fill the hole in the inner shell. During the relaxation the electron emits a characteristic x-ray to compensate for the energy difference between the two shells. The figure is adapted from ref. [33]

the photon energy (X-ray) elemental characteristic, and the elemental composition can be known by detecting the emitted photons. The complete range of the electronic transitions is illustrated in figure 2.11. However all the transitions are not detectable as the commonly used detectors cannot distinguish between the subshells. The X-ray photons are detected by one or more semiconductor detectors placed above and beside the sample in close proximity, and the signals are processed to generate an X-ray spectrum of the area of interest. [33]

EDX is performed in STEM mode and an area, line or point analysis can be performed where the probe is scanning in chosen fashion. The resolution of EDX is dependent on the resolution from the STEM and also by the type and design of the detector and area around it. EDX analysis is a fairly fast and easy-to-interpret technique in order to achieve general information about the elemental composition. The technique should not be used as the primary method to analyze lighter elements (Z<11). This is because the probability of emitting X-rays versus Auger emission decrease with lower atomic number. However, another technique available to analyze the lighter elements is electron energy loss spectroscopy (EELS), where the inelastically scattered electrons are detected instead.[33].

The EDX analysis generates an X-ray spectrum where the detected energies appear as peaks or lines. The spectrum should be qualitatively analyzed which can be done with an EDX software or manually. However, the peak identification by the software is not entirely trustworthy since some elements' peaks are very close in energy, and also some artefacts are present. In order to avoid misleading results and confusions the peaks should be controlled by hand in addition to the software analysis. Subsequently a quantitative analysis can be performed where the area, line or point chosen are analyzed over a longer time. One X-ray photon at a time is processed by the detector and hence a high number of counts are essential in order to achieve a representable result. As the area, line or point chosen are exposed repeatedly to a focused electron beam the material may be damaged which should be taken into consideration. [33]

2.5 Post-experiment data treatment

Image processing can be performed in order to enhance the intensity of the STEM micrographs. The atomic resolution HAADF STEM images were deconvolved to remove the effect

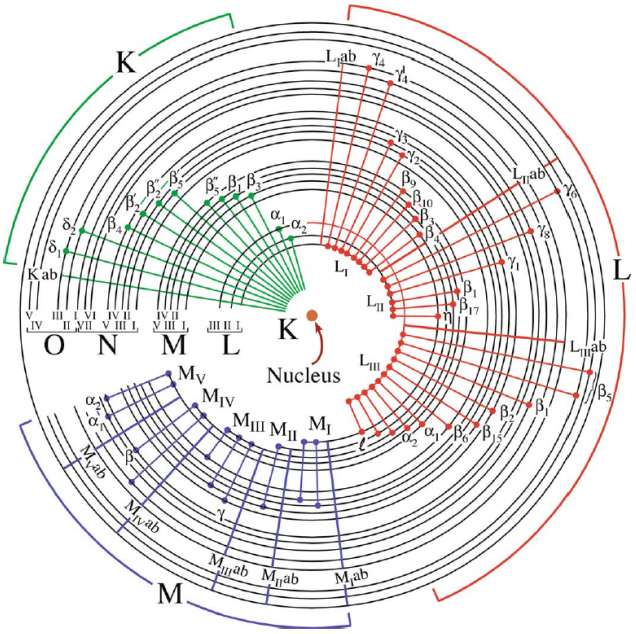

Figure 2.11: The figure shows the full range of possible electron transitions. All transitions are not possible to detect as the detector cannot distinguish between subshells. The figure is adapted from [33].

of the probe. This was performed in order to enhance the atomic resolution to distinguish the dumbbells. The deconvolution was performed by applying the iterative maximum entropy deconvolution algorithm described in ref. [36] with the STEM_CELL software tool.

Chapter 3

Experimental procedures

3.1 Material synthesis

The nanowire samples were synthesized at Lund Nano Lab at Lund University. The analyzed samples in this thesis are the following;

The crystal structures of the core is indicated in parenthesis for sample A and B.

A) InAs(WZ-ZB)-GaSb core-shell nanowires

B) InAs(WZ-ZB-WZ)-GaSb core-shell nanowires

C) InAs-GaSb core- shell nanowires; both core and shell in WZ structure.

- C1) InAs-GaSb core- (thin) shell nanowires
- C2) InAs-GaSb core- (thick) shell nanowires
- C3) InAs-GaSb core- (thick) shell nanowires

D) InAs-GaSb-InAs core-shell-shell

The samples are grown by means of metal organic vapor phase epitaxy (MOVPE) on (111) B InAs substrates pre-deposited with Au aerosol particles. For sample A, B and C3 the 40 nm Au particles were utilized and for sample C1, C2 and D the 30 nm Au particles. The InAs core was first grown and trimethylindium (TMIn) and arsine (AsH_3) were employed as the group III and V precursors. The GaSb was grown by trimethylgallium (TMGa) and trimethylantimony (TMSb). The molar fractions and III/V ratios were altered to change crystal structure between zincblende (ZB) and wurtzite (WZ). The V/III ratio was similar for all the GaSb growths; however the total mass flow rate was 1 order of magnitude lower for sample A and B than for C and D. The GaSb growth time for sample C1 was 15 minutes. The GaSb shell growth time for sample C2, and C3 was 40 minutes. Sample D was based on the thick shell sample C2 and the GaSb was grown for 40 minutes before the InAs shell.

Figure 3.1: A schematic structural overview of the type of nanowire. The desired structure is the WZ InAs-GaSb(-InAs) core-shell(-shell) nanowire, and the axial segment of GaSb is a result of the shell growth.

3.2 Electron microscopy

All the samples have been analyzed by means of transmission TEM and STEM imaging. A few nanowires from each sample were characterized if nothing else is specified. The analyzed nanowires are chosen in such fashion that they are considered to be representable for each sample. The composition was analyzed with EDX spectroscopy. The acquired micrographs and data have been processed in order to gain a structural understanding about the different nanowires.

After the growth of the nanowire an initial overview was acquired by a SEM (Zeiss LEO 1560). The SEM image was used to confirm that the growth had been successful in producing nanowires. The samples were mechanically transferred to Cu grids with a cover of lacey carbon prior to TEM imaging. All the samples were first analyzed by means of a JEOL 3000F TEM at Lund University (nCHREM), operating at 300 keV. The JEOL 3000F TEM is equipped with a Schottky FEG and has a maximum point resolution of 0.17 nm in TEM mode. The double tilt sample holder was used and the specimen stage was tilted to orientate a nanowire of interest to the right zone axis in order to allow for HRTEM imaging. The HRTEM imaging was performed to attain crystallographic information of the samples and the images were acquired by a 2x2k charge-coupled device (CCD) camera. The elemental analysis was performed by the JEOL 3000F TEM running in STEM mode, which has a maximum point resolution of 0.13 nm. The characteristic X-rays were detected by a silicon drift detector (SDD) based Oxford XEDS detector. The Oxford software INCA was used in order to process the EDX data.

Sample C1, the InAs-GaSb core-(thin)shell and D InAs-GaSb-InAs core-shell-shell nanowires were further analyzed by an aberration corrected FEI Titan^3 60-300 S/TEM at Ångströmhuset at Linköping University in addition to the initial TEM analysis performed by JEOL 3000F TEM. The Titan^3 60-300 S/TEM was equipped with image and probe C_s correctors and a monochromated high brightness FEG. The microscope has a spatial resolution near 0.6 Å at 300 keV in both TEM and STEM modes. Both the imaging and EDX spectroscopy were performed in high resolution STEM (HR-STEM) mode with a HAADF detector for imaging. The characteristic X-rays were detected by Bruker's Super-X EDX detector, which is comprised of four SDDs and have a large collection angle. The EDX analysis with this microscope will be referred to as high resolution EDX.

3.3 Post-experiment data treatment and micrograph analysis

The STEM micrographs acquired by the aberration corrected Titan^3 60-300 S/TEM was deconvolved to remove the effect of the probe in order to enhance the intensity. This was performed by applying the iterative maximum entropy deconvolution algorithm described in ref.[36] by using the STEM_CELL software tool.

The micrographs acquired with the JEOL 3000F TEM were analyzed with the ImageJ and Digital Micrograph software tools. FFT-analysis was performed on interesting areas of the HRTEM images to determine the crystal structure and atomic distances of the material. To confirm the crystal structure observed in the FFT, the software tool Carine was used to process the measured distances and identify the crystallographic planes. Carine was also used to model the unit cells and DPs of the crystal structures.

The mass-thickness contrast and the Z-contrast were investigated by intensity profiles over the structure to determine the cross section thickness and the polarity of the dumbbells.

Chapter 4

Result and Discussion

InAs-GaSb heterostructured nanowires are analyzed by means of TEM and the results are presented in this chapter. The analyzed nanowires are from six samples which are grown under different growth conditions yielding different structural properties. The structure and physical properties of sample A, B, C2 and C3 will be described briefly. We will focus on the properties of two of the samples, C1 and D, and additionally elaborate on their structural properties at the heterointerfaces.

Figure 4.1 shows a structural overview of the investigated samples.

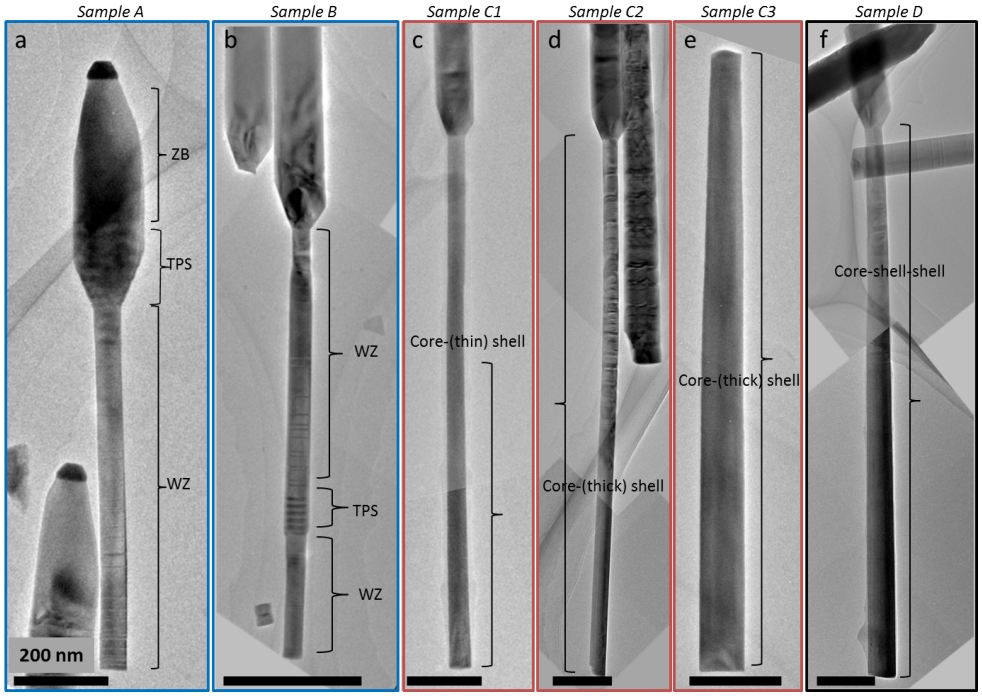

Figure 4.1: Low magnification TEM micrographs visualizing one representable nanowire from each sample (a-f). Sample A and B (a, b) have a core of alternating WZ and ZB structure, which is indicated in the respective image. The WZ InAs-GaSb core-shell samples, C1, C2 and C3, are shown in image c, d and e. The double shell structure, sample D, is shown in image f. The ZB axial growth is not shown in image (b-f) as the core-shell structure is of interest in this thesis. a) InAs-GaSb (WZ-ZB) core-shell, b) InAs-GaSb (WZ-ZB-WZ) core-shell, c) InAs-GaSb core-(thin) shell, d) InAs-GaSb core-(thick) shell grown from 30 nm seed particles, e) InAs-GaSb core-(thick) shell grown from 40 nm seed particles, and f) InAs-GaSb-InAs core-shell-shell. The scale bars are 200 nm.

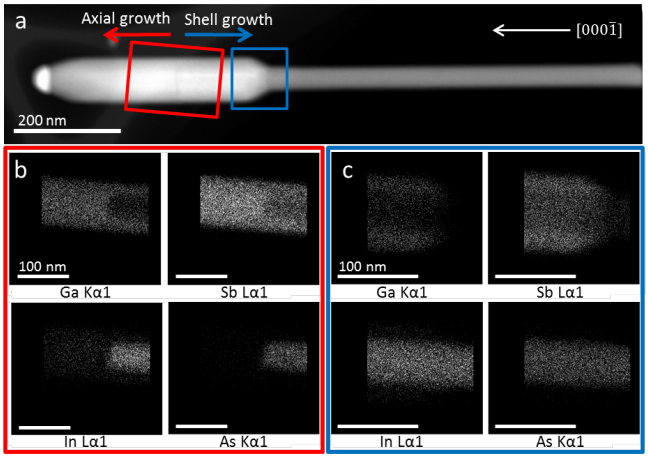

Figure 4.2: (a) A STEM image of one of the analyzed nanowires from sample A and the EDX mapping from two areas of interest; (b) the end of the InAs core and start of the GaSb shell and axial growth (red), and (c) where the GaSb shell ends (blue). The arrows indicate the growth direction of; the nanowire (white), the axial GaSb segment (red) and the GaSb shell (blue).

4.1 InAs-GaSb (WZ-ZB) core-shell nanowires (Sample A)

The sample is comprised of nanowires with a long segment of InAs WZ core, with a thickness of around 55 nm, which ends with a short TPS segment as seen in figure 4.1(a). The TPS segment is observed by EDX analysis to be overgrown by a GaSb shell forming an InAs-GaSb core-shell segment, see fig. 4.2.

HRTEM images of the bare WZ InAs core and the InAs-GaSb TPS segment is presented in figure 4.3(b,c). The WZ InAs remains bare and no GaSb shell forms on it. The shell growth is attributed to the different surface energies of ZB and WZ [37]. The surface energy of the ZB {110} facets in the TPS segment is higher than the one of {11$\bar{2}$0} facets of WZ. Therefore, the TPS segment appears to have the shell growth induced where the atoms may have diffused from the axial growth. The phenomenon of crystal phase selective shell growth has been reported for GaSb on ZB InAs [21], as well as for similar III-V nanowires [38]. The phenomenon of ZB induced shell is also observed more clearly in sample B.

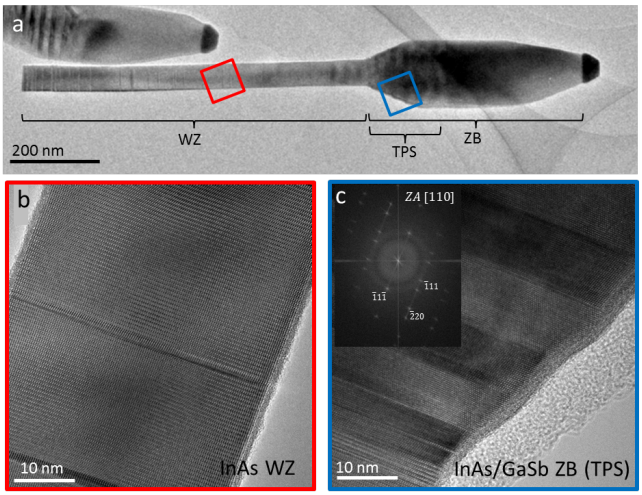

Figure 4.3: (a) A low magnification TEM micrograph of sample A. The red and blue boxes indicate the areas where the (b, c) HRTEM images were acquired. (b) The InAs WZ core is observed to not have a shell which is consistent with the EDX analysis. (c) The core-shell interface is difficult to distinguish in the HRTEM image of the TPS segment due to the weak interface contrast of ZB on zone axis [110]. The inset shows the FFT of the TPS segment.

4.2 InAs-GaSb (WZ-ZB-WZ) core-shell nanowires (Sample B)

The analyzed nanowires from this sample have a core of InAs which have; first a segment of WZ, followed by a short ZB TPS segment and finally another WZ InAs segment. The structure ends with an axial segment of ZB GaSb. The GaSb shell covers the TPS and the second WZ segments.

The shell tapers along the second WZ segment until a shell no longer can be distinguished, which is presented in figure 4.4(a-d). The thickest shell is on the TPS segment (~8nm), however, a sharp core-shell interface cannot be observed due to the weak interface contrast of the ZB segment from [110] zone axis (fig 4.4b). FFT analyses of the HRTEM images in order to confirm the crystal structures of the WZ segment and the TPS segment have been performed and are shown in figure 4.4(b, c) and 4.5(c, d).

The thinner GaSb shell on the second WZ segment is assumed to be induced by the TPS segment, due to a higher surface energy of the ZB facets than the ones of WZ. The TPS segment acts as nucleation point, and the shell continues on to the WZ segment in the direction of the axial segment. The shell ends a short distance below the GaSb axial segment, which indicates that the axial growth does not induce the formation of a shell if no TPS segment is present as in sample A. The direction of the shell growth, as well as the small tapering in the growth direction, indicates that the atom diffusion from the surface is determining the shell growth rather than nucleation and step flow along the sidewalls. A thin shell on one side of the first WZ segment could be present below the TPS segment; however the interface contrast is too low in the HRTEM images to be able to determine it precisely.

In addition the shell appears to behave differently at the TPS segment depending on the side, which is presented in figure 4.5. This asymmetry is observed at the interface between the first WZ segment and the TPS (Fig.4.5b). One of the ZB facets appears to have induced a thin shell on one side of the first WZ segment but not on the other side. This observation of an asymmetric shell in downwards direction indicates that the ZB facets affect the shell growth differently. An asymmetric shell along the opposite growth direction was also found for sample C1.

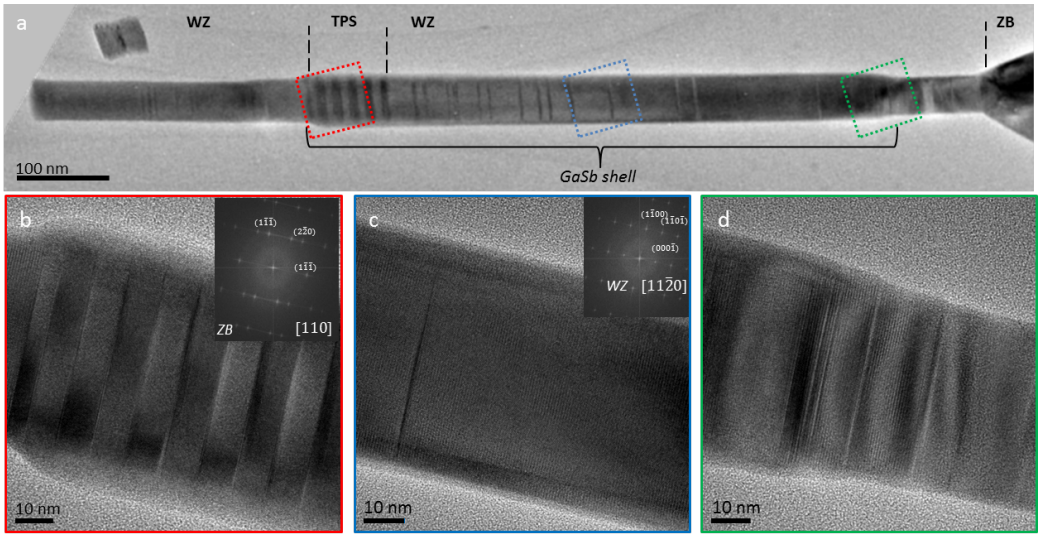

Figure 4.4: (a) A low magnification TEM micrograph of the InAs-GaSb (WZ-ZB-WZ) core-shell structure. The boxes indicate where the (b-d) HRTEM images have been acquired. A ∼8nm shell is seen on the (b) TPS segment, which tapers and are ∼5nm in the (c) middle of the second WZ segment. (d) The end of the shell is observed close to the axial growth. The FFTs of the HRTEM images (b-c) are shown as insets in each image.

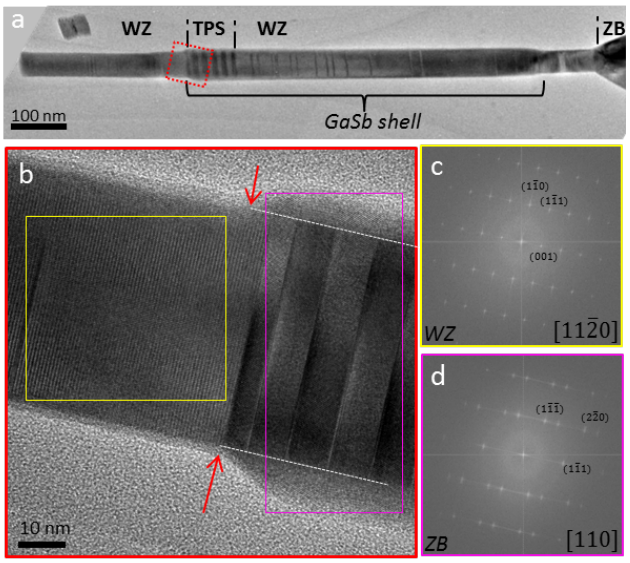

Figure 4.5: The figure show; (a) an overview of the core-shell structure of sample B and (b) a HRTEM image acquired at the first WZ-TPS interface (red inset in (a)) of InAs-GaSb core-shell sample. The FFT of the (c) WZ and (d) TPS segment are acquired on zone axis [11$\bar{2}$0] and [110]. The white dashed lines in (b) indicate the assumed core-shell interface and the red arrows indicates the supposed start/end of the shell and are observed to differ in appearance depending on the side, i.e. ZB facet.

4.3 InAs-GaSb core- (thin) shell nanowires

Three different samples of InAs-GaSb core-shell nanowires (C1, C2, and C3) with different GaSb shell growth times have been analyzed. A thorough TEM analysis of the sample with the thinner GaSb shell (sample C1) has been performed. The structure and structural issues such as stacking faults, morphology of the shell, composition and investigation of the axial and the radial interface will be discussed.

The sample is comprised of nanowires with an InAs core with a thin GaSb shell on the bottommost part and an axial GaSb segment. A schematic of this is seen in 4.6.

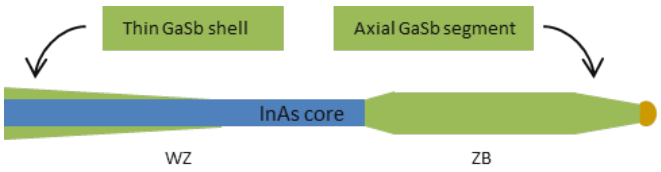

Figure 4.6: A schematic of the nanowires from the InAs-GaSb core- (thin) shell sample.

HRTEM micrographs were acquired to investigate the core-shell structure and are presented for one of the nanowires in figure 4.7. The HRTEM micrographs show the interface between the core structure and the shell. The thickness of the shell is observed to decrease (taper) along the growth direction [000$\bar{1}$], until the visible interface ends roughly in the middle of the nanowire. The end of the shell could not be determined precisely by HRTEM imaging due to the gradual tapering of the shell. A very thin shell could possibly still be present while not distinguishable due to the decrease in interface contrast as the shell thickness decreases. In addition neither could a shell be observed in the HRTEM images of the upper part of the wire, see figure 4.8. However, elemental analysis is required to confirm these observations.

The thickness of the core was uniform and measured to be $\sim$40 ($\pm$1) nm, and the length was around 1.1 to 1.9 μm for the examined nanowires. The thickness of the shell was measured (Fig. 4.7) to vary from 13 nm at the thickest part and decrease to 1-2 nm at the thinnest part. In addition it differs slightly between the two sides.

The shell is fully epitaxial and adapts the crystal structure of the core as well as the stacking faults. No exceptions have been found in any of the observed nanowires. No misfit dislocations could be found throughout the analysis of all images acquired on the core-shell sample even though the lattice mismatch for WZ InAs-GaSb is 1.15%.

4.3.1 Stacking faults

The FFT of the bare core of the nanowire is obtained from a HRTEM image in figure 4.8 showing the WZ structure. A single stacking fault of a bilayer "C" is also present and can be seen in the figure 4.8(a,b). The general observation of the nanowires was that the density of line defects is the highest in the vicinity of the base of the nanowire, and decrease along the growth direction.

This is a common observation for epitaxially grown nanowires. An example of this observation has been made in a GaAs WZ system [39]. This phenomenon is due to rapid fluctuations of the supersaturation of the seed particle in the beginning of the growth, i.e. when the material flux is increased as it both comes from the substrate surface as well as from the incorporation of atoms in the seed particle. This increases the total amount of stored energy which induces stacking faults to release the excess energy. However this event is described as a momentary change as the seed particle regains its previous configuration after a few bilayers of stacking fault, and the nanowire returns to its WZ structure.[39]

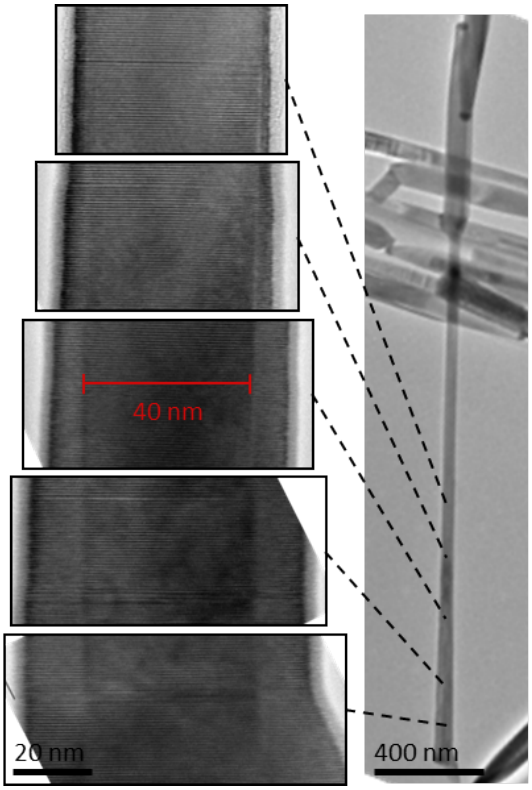

Figure 4.7: The HRTEM micrographs (left) of the nanowire (right) reveal the core-shell structure as well as the tapering of the shell which is observed along the growth direction.

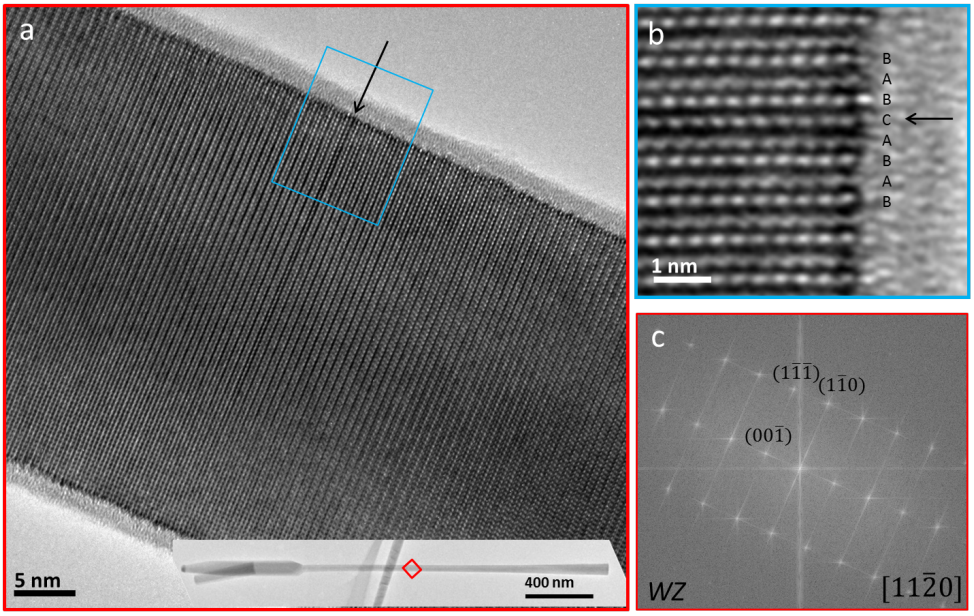

Figure 4.8: (a) A HRTEM image of the area where a stacking fault can be observed. The stacking fault is marked with the black arrow. The inset shows the whole nanowire and the red box indicates where the HRTEM image is acquired. (b) Higher magnification HRTEM image of the area of interest from (a). The stacking order is marked and the inset of the bilayer C can be observed. (c) The FFT of the HRTEM image confirms the WZ structure of the nanowire from [11$\bar{2}$0] zone axis.

4.3.2 Morphology of the shell

4.3.2.1 Tapering

Epitaxial radial growth on a nanowire core template can be employed to produce a uniform shell along the wire. However, tapering of the shell have been observed [40]. The growth of GaSb in WZ structure instead of ZB is a bit more challenging as ZB is the preferred crystal structure of the compound [11][22]. As a consequence the growth conditions needs to be adjusted.

In addition the surface energy of WZ is lower than the one of ZB, where radial growth is well known in the literature [41][21]. The lower surface energy adds to the difficulty of achieving a shell on WZ nanowires. To achieve the WZ GaSb shell the mass flow rate of the growth material had to be increased by one order of magnitude compared to ZB shell growth parameters for sample A and B. Despite the increase in mass flow, only a thin shell could be achieved which does not even cover the whole nanowire. However, a tapering of the shell is observed and an explanation for this might also be found in the lower surface energy of WZ in comparison to the ZB.

Shell growth occurs via vapor-solid (VS) mechanism (section 1.1.3). In this mechanism the adatoms are collected in different ways. They can be collected either from the substrate or the base and diffuse upwards onto the side facets from the base of the nanowire. They can also find a kink on the side facets and continue collecting more adatoms causing step flow[42]. These are well known mechanisms which are reported for GaAs, InAs and InAsSb [41] and results in a uniform shell.

For pure WZ structure the nucleation of adatoms on the sidewalls can be argued to be less favorable due to the lower surface energy attributed to WZ than ZB for III-V nanowires [37]. However, as discussed earlier the density of stacking defects are higher at the bottommost part of the wire. This result in areas with higher surface energy, hence adatoms can be assumed to favor nucleation here. In addition, at the vicinity of the base of the wire the number of shell atoms diffusing from the substrate is higher which increases the probability for shell growth. The axial growth may also compete with the shell growth by means of collecting the shell material, which also could affect the lack of shell near the interface.

These assumptions could explain the favored presence of a shell on the lower part of the nanowire as well as the tapering effect that is observed. The diffusion rate and the unfavorable nucleation of shell atoms on the sidewalls of the wire could also explain why the shell is not covering the whole nanowire. The growth time of 15 minutes could be argued to be too short for the shell atoms to diffuse along the whole nanowire creating a covering shell of GaSb. For the InAs-GaSb core-(thick) shell and the InAs-GaSb-InAs core-shell-shell structure a longer growth time is employed which will be seen to change the appearance of the shell (section 4.4 and 4.5).

The tapering of the shell has been observed to 'generally' coincide with stacking faults in these InAs-GaSb core-shell nanowires. This can be seen in figure figure 4.9. However, the stacking faults are not always observed at tapering events of the shell. This phenomenon for WZ nanowires has been reported before. Plante and Lapierre have shown that faults generally coincide with surface steps on the sidewall surface of bare WZ nanowires.[39]. This stepwise tapering effect is not observed for the InAs WZ core, which should be due to the high degree of control of the growth of InAs WZ nanowires [43][44][45].

4.3.2.2 Effect of Zincblende facets on the shell growth

A "one-sided shell" in proximity to the axial GaSb segment was found in one of the analyzed nanowires and is shown in figure 4.10(a-b). The shell continues downwards until it is terminated at a stacking fault. This correlates to the previous discussion about the tapering of the shell due to stacking faults. An explanation to the one sided shell could be due to the polarity of the different ZB facets of the axial segment. Polarity-driven effects on shell growth have

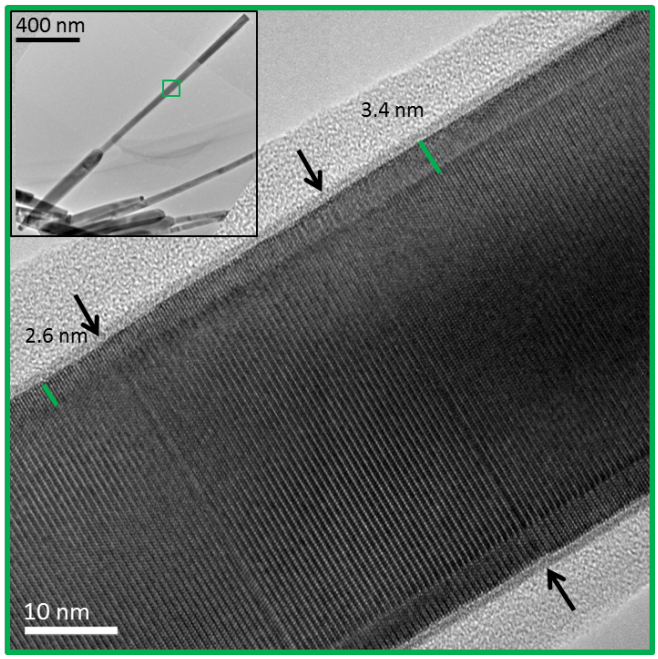

Figure 4.9: The stacking faults in correlation with tapering, indicated with black arrows. The area from where the HRTEM image is acquired is marked in the inset of a low magnification TEM micrograph.

been observed for InGaAs system [40], where the different polarities of the ZB facets seem to alter the shell-inducing properties. Considering the orientation of the nanowire on zone axis $[11\bar{2}0]_{WZ}/[110]_{ZB}$, we have two types of facet of ZB facing upwards the electron beam in connection with the WZ core as seen in figure 4.11. It has been observed that the ZB facets of the axial segments are not symmetric on zone axis [110], which is presented and illustrated in figure 4.11 as well. The angle of the two facets corresponds to the {111} and the {001} planes. Apparently {001} facets induce shell growth downwards to the InAs WZ. Therefore, we expect a 3-fold symmetry of the shell in this region. The composition of the shell of the same nanowire was in addition analyzed by means of EDX which is described in the next section.

4.3.2.3 Chemical composition

Qualitative EDX analysis of the nanowire with the previously mentioned ZB-induced asymmetric shell was also performed. The results are presented in figure 4.12. An axial line scan of the core-shell structure was performed and the signal from the GaSb shell is detected to be strongest at the bottom of the wire. The Ga and Sb signals decrease along the growth direction of the wire (Fig. 4.12a), in agreement with the observations made from the HRTEM analysis (section 4.3.2). Radial line scans was acquired at the; bottom of the nanowire (Fig. 4.12c), the middle of the nanowire (Fig. 4.12d) and close to the axial segment (Fig. 4.12e). A clear signal of the GaSb shell was observed in the bottommost part of the wire (Fig. 4.12c). In the middle of the wire signals from GaSb were detected on one side of the wire while only Ga signal was detected on the other (Fig. 4.12d). The Ga and Sb signals had in addition decreased compared to the radial line scan at the bottommost part. This is consistent with the observed and discussed tapering of the GaSb shell (section 4.3.2.1). The radial line scan in close proximity to the axial segment validates the observation of an asymmetric shell (section 4.3.2.2), as no Ga or Sb signal was detected on the 'bare' side as seen in figure 4.12(e).

Additionally, a radial line scan was performed on another nanowire where no shell could be distinguished in the HRTEM images, which is shown in figure 4.13. Weak signals of Ga and Sb ware detected at the upper part of a nanowire (Fig. 4.13b). However, no shell could be observed in the HRTEM image acquired on the same area (Fig. 4.13c).

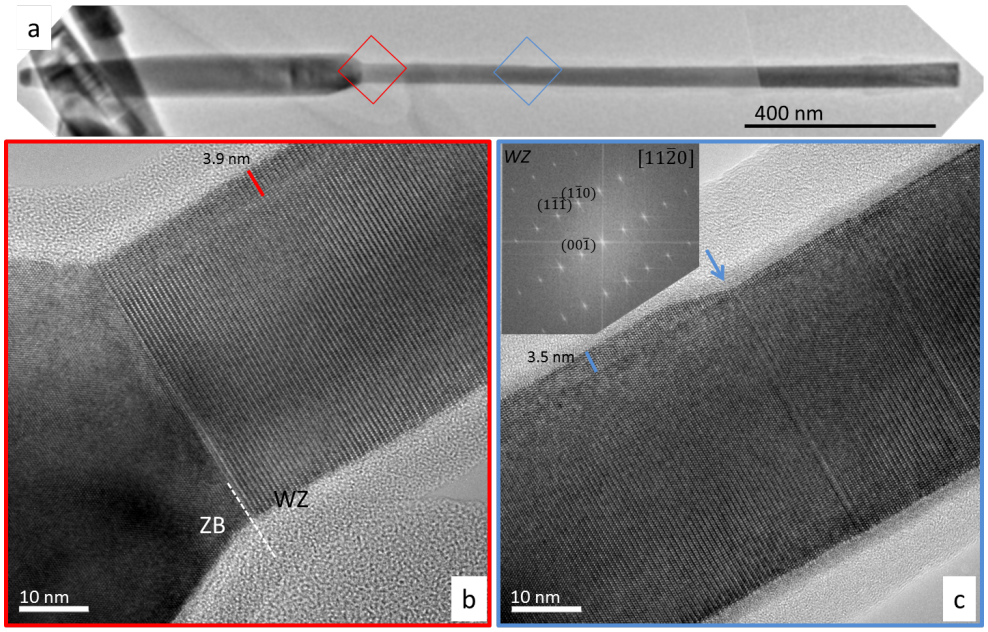

Figure 4.10: (a) A low magnification TEM micrograph of the nanowire where a ZB-induced shell was found on one side. The areas where the (b, c) HRTEM images of the ZB induced shell were acquired are marked in the (a). In (c) a blue arrow indicates the stacking fault which seem to correlate with the termination of the shell.

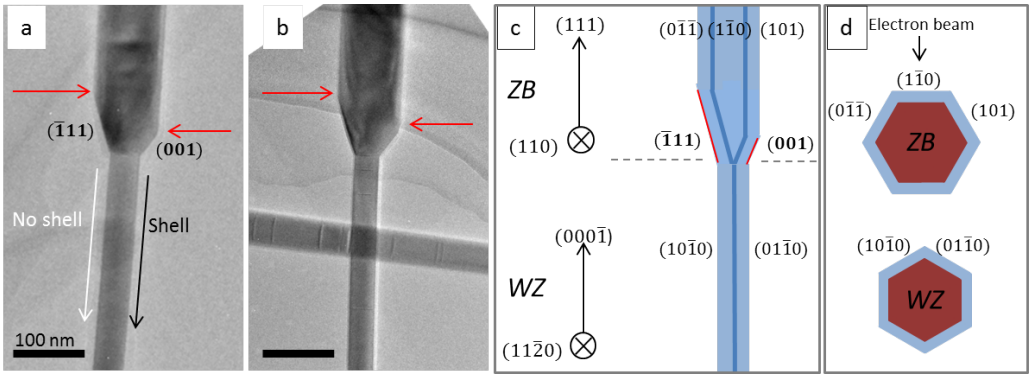

Figure 4.11: The axial segment interface for two nanowires of the core-shell samples is presented in (a-b). The red arrows indicate where the facets that connects to the WZ core ends. The nanowire imaged in (a) have an asymmetric shell which is presented in figure 4.10 and indicated here as a black arrow. The facets are marked in image (a) where the (001) facets induce the shell. No shell close to the interface was observed for the nanowires imaged in (b). (c) A schematic of the facets of the axial interface which correponds to the images (a-b) are presented with the growth direction, zone axis and facets indicated. (d) The cross sectional structure with the facets that corresponds facets facing the electron beam of the shematic in (c) are marked.

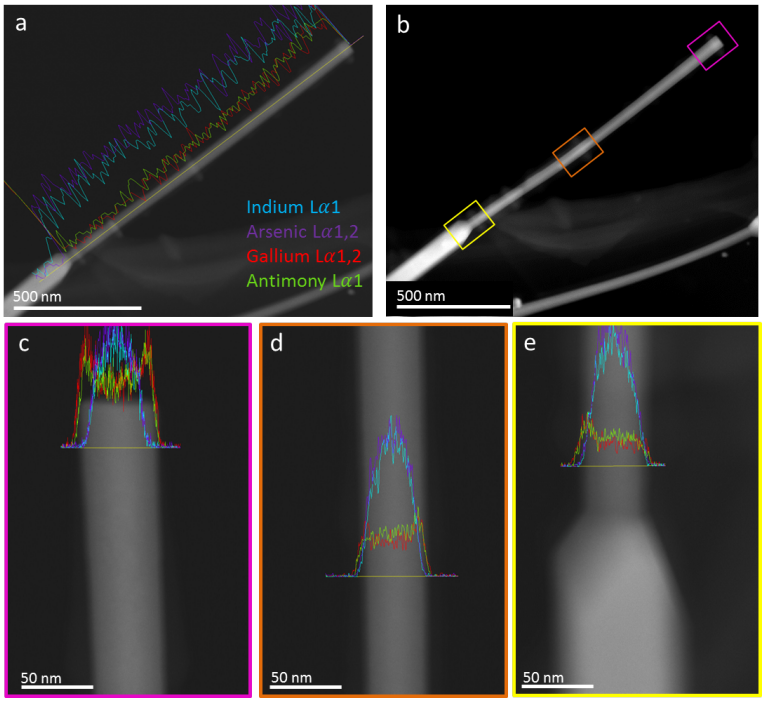

Figure 4.12: The EDX analysis from the core-shell nanowire with an asymmetric shell near the axial growth. A line scan acquired over the whole nanowire is seen in (a). Line scans are acquired over the: (c) bottom of th e nanowire, (d) middle of the nanowire and (e) asymmetric shell. The images (c-e) correspond to the colored boxes in the low magnification STEM image (b).

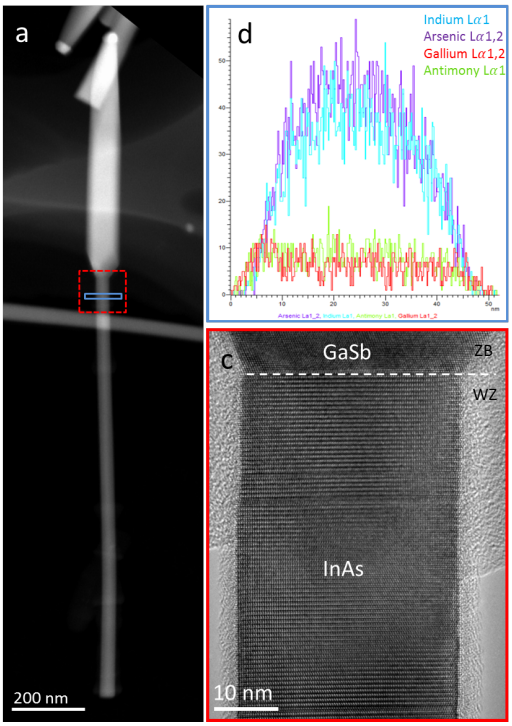

Figure 4.13: The area from which an (b) EDX line scan was performed and a corresponding (c) HRTEM image from the same area is indicated in blue and red in the (a) STEM image.

4.3.2.4 Ga oxide on the bare InAs core

High resolution EDX analysis was performed on the 'bare' InAs core (Fig. 4.14a) in order to clarify the possible presence of a thin shell. The EDX mapping of the area close to the axial segment shows strong signals of Ga and O from the amorphous layer around the upper part of the nanowire, as presented in figure 4.14(b,c,f,g). A shell had not been distinguished in the HR-STEM image of this area (Fig. 4.14b). This indicates that on the part where the InAs core lacks a surrounding shell, an amorphous Ga oxide layer is present instead.

The Ga oxide is argued to have formed after the growth as oxygen is not present during the growth. A hypothesis is that the Ga oxide originates from a very thin GaSb shell which has been oxidized directly after growth and induced a migration of Sb. The Ga oxide was observed on both sides of the bare InAs core near the GaSb axial segment. However this Ga oxide was not seen on the lower parts of the nanowire where a thicker GaSb shell was present.

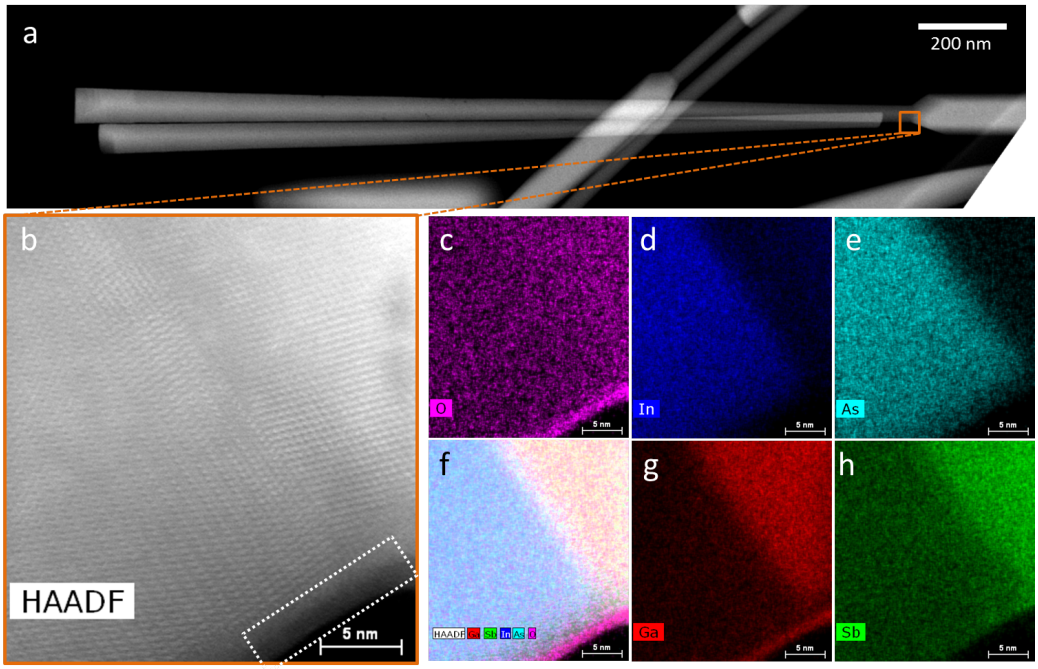

Figure 4.14: High resolution EDX analysis of one side of the nanowire close to the GaSb axial segment. (a) A low magnification STEM image marking the analyzed area in orange. (b) A HR-STEM image of the area of interest, (c-h) EDX maps. The amorphous layer is indicated with the dashed white box. All the EDX maps are overlaid in image f. The Ga-rich oxide can be seen on the side the respective image and in (g) Ga in red and (c) O in pink.

4.3.3 The radial interface

4.3.3.1 Composition and polarity

The InAs-GaSb core-shell nanowires were also analyzed with aberration corrected STEM which due to Z-contrast revealed a dark layer at the core-shell interface, which can be seen in figure 4.15. This darker interface was seen along the core-shell structure and is homogenous in thickness (one atomic bilayer) and intensity. Due to the Z-contrast (section 2.2.4) heavier compounds will appear brighter in the STEM images and as the atomic weight of InAs and GaSb are the same, another lighter compound is assumed to create the darker interface. Among the four elements, Ga and As are the lighter. Therefore, firstly GaAs is assumed to be present at the interface based on the intensities in the image (Fig. 4.15). This phenomena is further

investigated by intensity profiles of the dumbbells visible in the atomic resolution HAADF STEM image presented in figure 4.16.

In atomic resolution HAADF STEM images the polarity of the core and shell can be determined based on Z-contrast [12]. From the intensity profiles (Fig. 4.16) the InAs core is observed to be As-polar (anion-polar) as the lower intensity peak is in top position along the growth direction (Fig. 4.16b). Similarly, the shell is Sb-polar (anion-polar) as the higher intensity peak is in top position (Fig. 4.16d).

Based on the same argument, the lower and the slightly higher intensity peaks of the interface profile (Fig. 4.16c)should indicate Ga and As, respectively. However, this would place Ga in top position, and the interface would be cation-polar. This is likely not the case since a polarity inversion is energetically unfavorable [46][47]. In case of a cation-polar layer at the radial interface between the core and the shell, there would be two polarity inversions; anion-polar to cation-polar and back to anion-polar, which is highly unlikely. If GaAs is present at the interface, it should still be anion-polar, i.e. placing As at the top position of the dumbbell.

The anomaly in the intensity profile can be explained by addition of over-and underlying atoms in the atomic columns of the interface. The intensity profile of the visible dumbbell is in fact the average of the atomic column. The appearance of the profile is then reasonable if considering that we do not have pure GaAs, rather a mixture of GaAs and InAs (i.e. a ternary of GaInAs). The alternation between Ga and In appears at the cation-position of the dumbbells which give rise to the enhanced intensity peak. This intensity effect is also present near the interface for the outer part of the core, which intensity is somewhat off for the As peak due to the contribution of the Sb atoms in shell above and below at the same position. This effect decreases further into the center of the core in relation to the increase of the core-shell thickness ratio.

The anion-polarity was determined in these nanowires over a few stacking faults as well as defect free areas and observed to be consistent.

The bilayer of GaInAs might be formed during or after growth. A similar phenomenon where an interface with a different contrast in core-shell structure has been reported [15]. Ganjipour et al found the interface between a ZB GaSb core and a ZB InAs shell to appear brighter and the reason for that was found to be an enhanced ratio of Sb in the interface. The proposed explanation was an enhanced Sb content immediately after the switch of precursors. Even if we do not see the same ternary composition in the two systems, is it likely that our interface composition is due growth parameters. This can be argued as the growth conditions for the two systems where different.

4.3.4 The axial interface

The axial interface between the InAs core and the GaSb axial segment was investigated by means of high resolution EDX (Fig. 4.17). This gives us more detailed information which reveals interesting features of the nanowires which could not be observed with normal EDX. The first observation made with the qualitative EDX analysis was that the axial interface between the InAs wire and the axial GaSb segment did not show a sharp interface. This could also be seen as a change in contrast in the corresponding HR-STEM images as there is a dark region at the beginning of the GaSb segment (Fig. 4.17b). However, EDX is needed to determine the chemical composition.

The EDX maps in figure 4.17(c-g) show that the As signal (Fig. 4.17d) is also observed on the other side of the axial interface where is supposed to be GaSb. Likewise, the signal from Sb is weak in an equally long distance from the interface into the axial segment (Fig. 4.17g). The signals from In and Ga end with respect to the axial interface as seen in figure Fig. 4.17(c, f). With this information the conclusion is that the first bilayers after the interface contain As which substitutes Sb (appearing darker in HAADF-STEM micrographs as As is lighter than

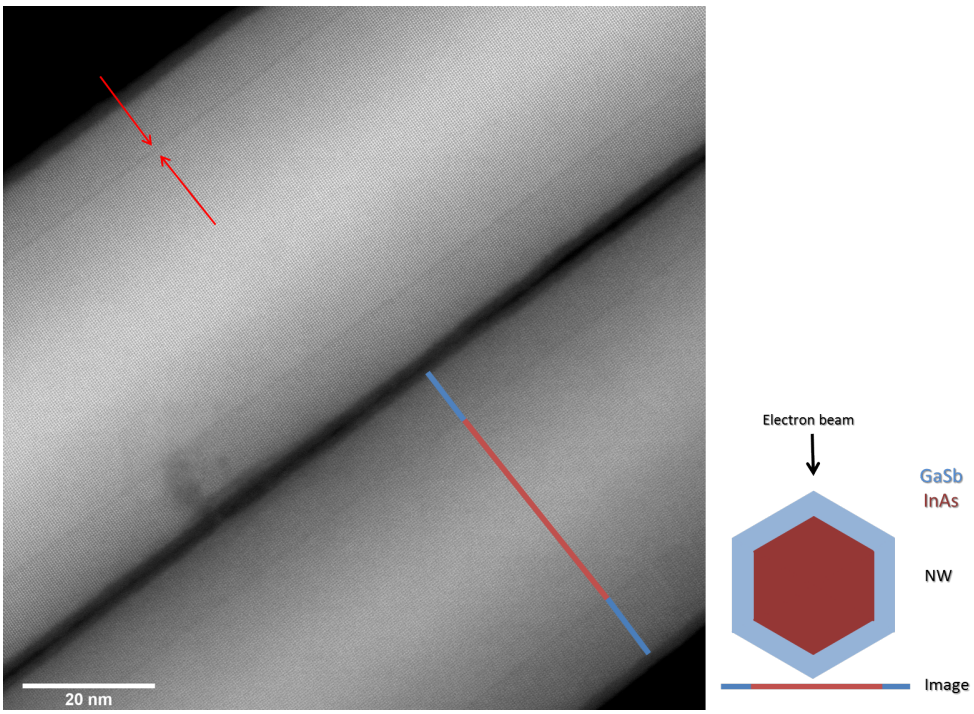

Figure 4.15: An atomic resolution HAADF STEM image where the interface of the core-shell structure can be seen as a darker layer, indicated by the red arrows. The cross section of the nanowire is illustrated and the corresponding final image where the shell and core are visualized in blue and red, respectively.

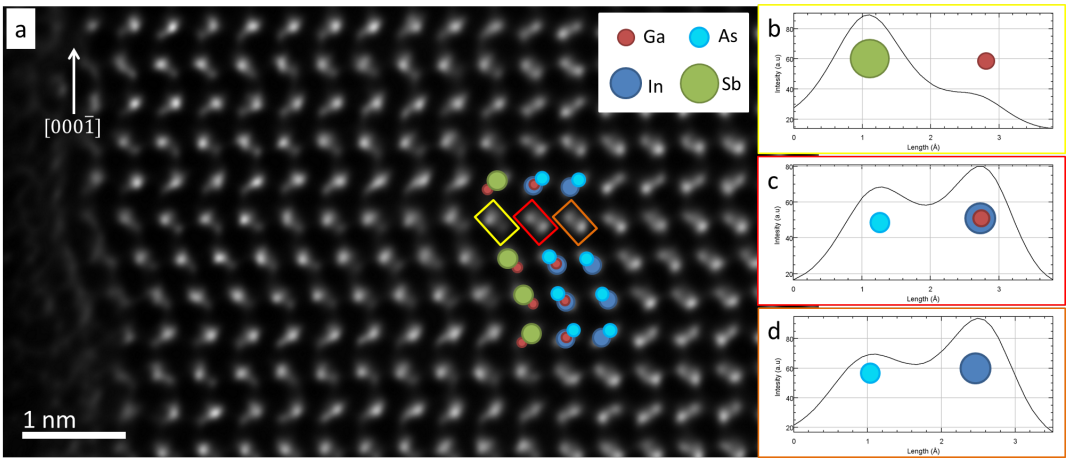

Figure 4.16: (a) The deconvolved HAADF STEM image of a stacking fault of in the core-shell nanowire. The insets show the intensity profile of one dumbbell unit,(b) the GaSb (yellow), (c) the interface comprised of a GaInAs ternary (red) and the (d) InAs (orange). The polarity is conserved throughout the core-shell-interface as well as throughout the stacking fault.

Sb) and probably we have a ternary GaAsSb compound. This is also validated by HAADF-STEM imaging as this area has the lowest contrast in the STEM image which is attributed to the two elements.

This short segment of changed composition is explained by the reservoir effect of the VLS growth mechanism and the solubility of Sb in Au which is higher than for As and other group V elements [19]. The elements are solved in the Au particle and when the precursor changes the elements are still present in some quantity in the Au particle. Depending on the solubility of an element in Au the time for supersaturation will differ. As Sb has a higher solubility in Au than As, it will take longer time for the seed particle to supersaturate with Sb. This leads to the seed particle being depleted of As before the Sb is incorporated in the growth [48].

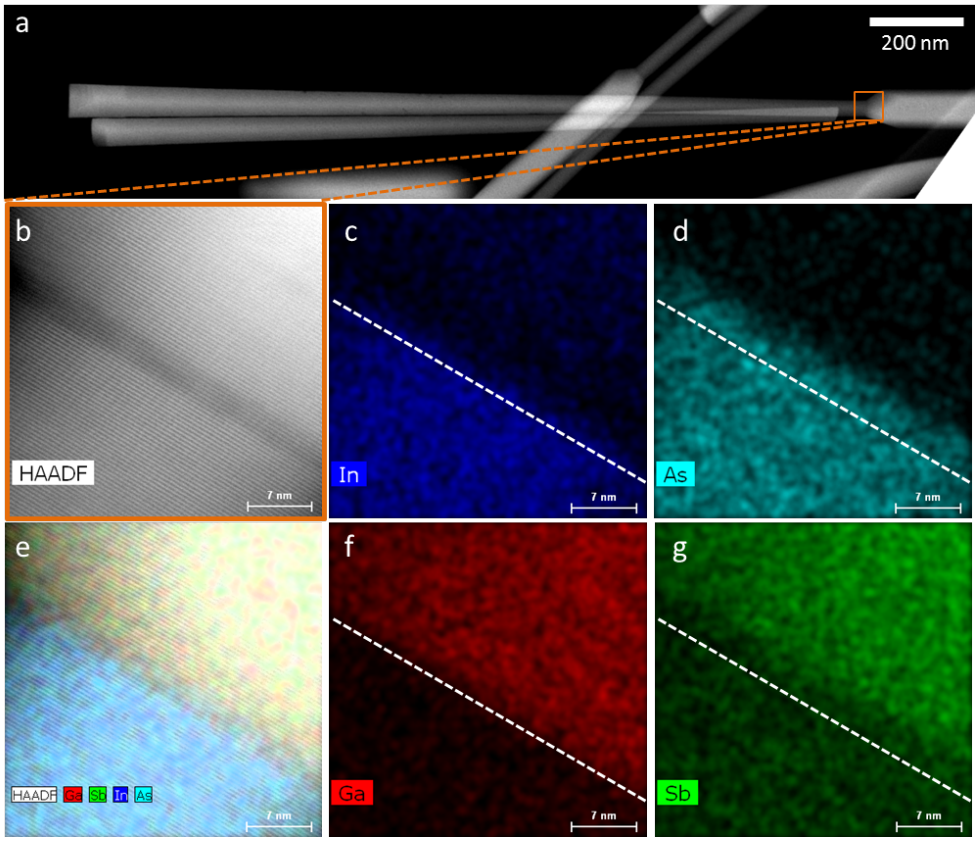

Figure 4.17: The EDX analysis of the axial interface in the core-(thin) shell nanowire. The analyzed area is marked in (a) and the corresponding HR-STEM is shown in (b). The EDX maps are (c-g) where (e) contains all elemental signals. The signal from In (c) and Ga (d) are observed to end right at the interface between the WZ core and ZB axial growth, marked with a white dashed line. The signal from As (d) is present an equal length as Sb (g) are lacking. This is due to the different solubility of the elements in the Au seed particle during the switch of the precursors.

4.4 InAs-GaSb core-(thick) shell nanowires

Two samples of InAs-GaSb core-(thick) shell nanowires grown from 30 nm and 40 nm seed particles, sample C2 and C3 respectively, have been analyzed by means of TEM. The structure and structural issues such as stacking faults and the morphology of the shell will be discussed. The InAs-GaSb core-(thick) shell sample grown from 30 nm seed particles is of interest as it is the reference sample of the InAs-GaSb-InAs core-shell-shell nanowires (section 4.5). The nanowires grown from 30 nm seed particles had a 1.7-1.9 μm long WZ InAs core with a thickness of 32-35 nm. The nanowires had a ZB GaSb axial segment as well as a GaSb shell along the full length of the core.

The analyzed nanowire grown from 40 nm seed particles had a 1.2 μm long WZ InAs core with a uniform thickness of 46-48 nm. A GaSb shell was observed along the whole core.

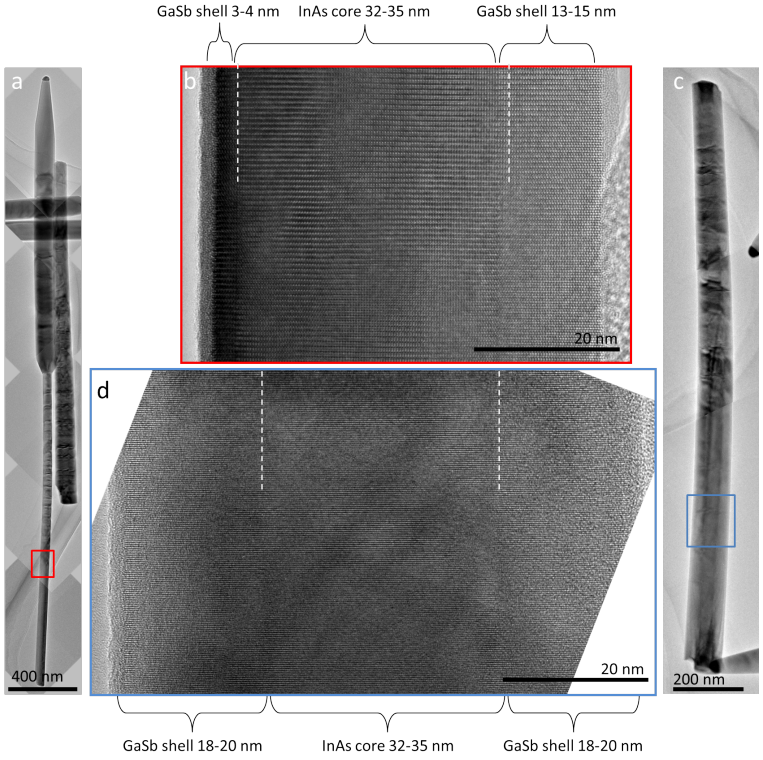

Figure 4.18: Two nanowires (a and c) from the InAs-GaSb core-(thick) shell samples was analyzed. Image a and b is acuired on the same nanowire and image c and d on another nanowire in the same sample. The first nanowire was observed to have different shell thicknesses depending on side (b), while the HRTEM image of the other nanowire (d) revealed a uniform shell thickness. This phenomenon was also found in the InAs-GaSb-InAs core-shell-shell structure. The difference in shell thickness was attributed to the presence of two different cross-sectional shell structures.

4.4.1 Morphology of the shell

The tapering of the GaSb shell of the 30 nm seeded nanowires is less prominent in this sample compared to the InAs-GaSb core-(thin)shell and the InAs-GaSb core-(thick)shell grown from 40 nm seed particles. However, the thickness of the GaSb shell was observed to differ between the sides in some samples and measured to be 3-4 nm or 13-15 nm depending on the side (Fig. 4.18a, b). The GaSb shell was measured to be 18-20 nm on nanowires with a uniform shell (Fig. 4.18c, d). This phenomenon with different shell thicknesses due to 3-fold and 6 fold symmetry in the same sample was observed in the InAs-GaSb-InAs core-shell-shell nanowires as well. This is further discussed in section 4.5.

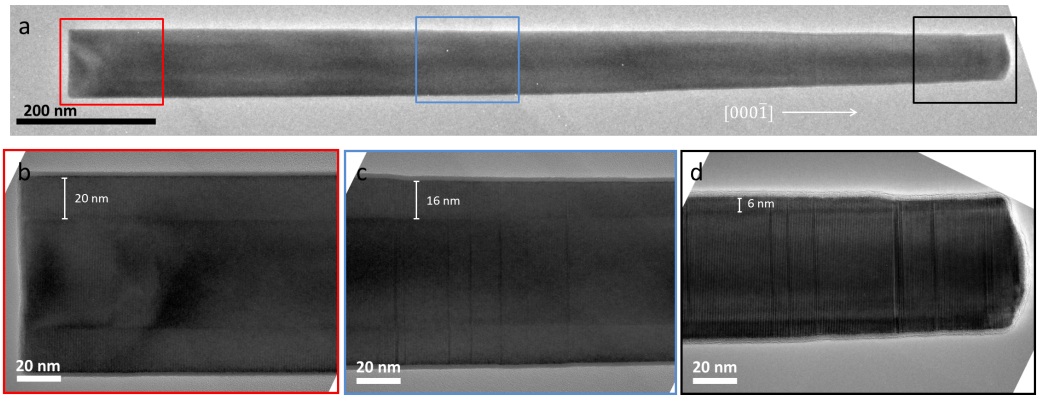

Figure 4.19: The tapering of the GaSb shell of the InAs-GaSb core-(thick) shell grown from 40 nm seed particles. The tapering can be observed in the low magnification image (a) as the thickness decreases in the growth direction. (b-c) Magnified areas of the nanowire where the decrease in shell thickness is more clearly seen. The nanowire is broken off and the axial segment should be located to the right of (d). As seen in (b-d) the thickness of the core is uniform and measured to be 46-48 nm.

The growth time of 40 minutes employed here have been enough to cover the InAs core with a full GaSb shell, in comparison to 15 minutes for the InAs-GaSb core-(thin) shell sample when a full shell could not be acquired. The shell growth time for various III-V core-shell nanowires found in the literature usually varies from a few of minutes up to around half an hour [15]. This concludes that a longer shell growth time is necessary to grow a full shell of WZ GaSb.

The nanowires grown from the 40 nm seed particles had a core of 46-48 nm. The shell was 20 nm at the bottommost part and tapered noticeable with the thinnest part of 4 nm, which is shown in figure 4.19(a-d). In the same figure it can also be observed that the analyzed nanowire had a uniform shell thickness on both sides.

However a high amount of stacking faults was found in this nanowire, especially closer to the axial segment. Tapering events of the shell were 'generally' found in correlation with these stacking faults. This is shown in figure 4.20(b-c). This phenomenon was also found for the InAs-GaSb core-(thin) shell nanowires (sample C1), however the stacking faults were fewer near the GaSb axial segment. The mechanism for tapering events at stacking faults was discussed in section 4.3.2.1 where the tapering was attributed to a diffusion limited VS mechanism. The shell atoms are accumulated on the substrate and diffuse upwards on to the nanowires and the stacking faults near the axial segment seem to somewhat hinder the shell growth. The distance from the substrate is a hinder itself as it takes longer time for the adatoms to diffuse further up the nanowire.

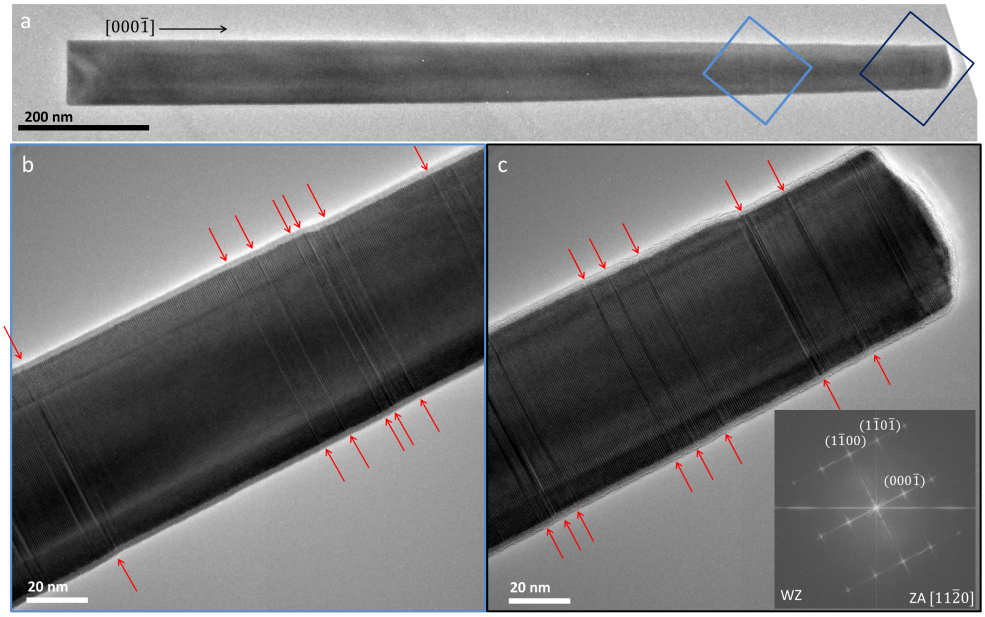

Figure 4.20: The figure shows the stacking fault of the InAs-GaSb core-(thick) shell nanowire grown from 40 nm seed particles. (a) Areas with a high amount of stacking faults are marked in the image and the HRTEM images from these areas are shown in (b) and (c). The tapering seems to be correlated to the stacking faults as marked with red arrows. The FFT of (c) is shown as an inset in the image with the WZ structure from zone axis [11$\bar{2}$0].

4.5 InAs-GaSb-InAs core-shell-shell nanowires

A thorough TEM analysis of the InAs-GaSb-InAs core-shell-shell structure has been performed. The structure and structural issues such as stacking faults, morphology of the shell, as well as elemental analysis and investigation of the radial interface will be discussed. An interesting observation of structural difference among the analyzed nanowires will also be discussed. The outer InAs shell is grown on nanowires grown with the same growth parameters as the InAs-GaSb core-(thick) shell sample discussed earlier (section 4.4). The structures are illustrated in figure 4.21.

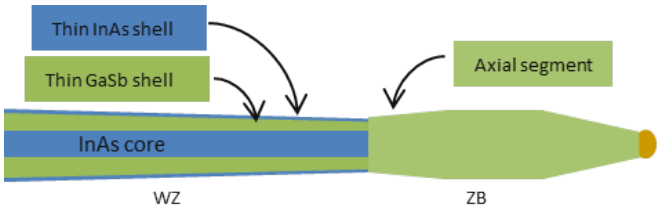

Figure 4.21: Schematic of how a double shell structure could be grown from an InAs-GaSb core-(thick) shell reference sample and an schematic of the double shell structure.

The SEM and TEM micrographs of a core-shell-shell nanowires are presented in figure 4.22(a, b). HRTEM images (one is shown in Fig. 4.22c) were acquired on the double shell structure and the WZ structure was confirmed by an FFT analysis (Fig. 4.22d).

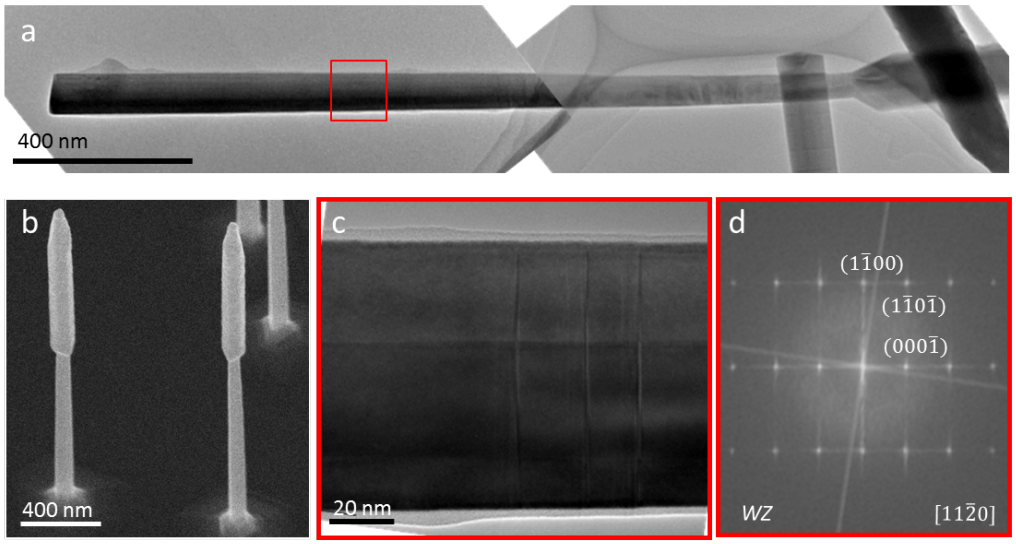

Figure 4.22: (a) A low magnification TEM micrograph and a (b) SEM image of a InAs-GaSb-InAs core-shell-shell nanowire . The red inset denotes where the (c) HRTEM image of the double shell structure was acquired .The (d) FFT of the (c) HRTEM image confirmed the WZ structure of the nanowire.

4.5.1 Morphology of the shell

4.5.1.1 Tapering

The crystal structure of the InAs-GaSb-InAs core-shell-shell nanowires was identified to be WZ, which can be seen in figure 4.22, and both shells are fully epitaxial. In addition to the crystal structure the stacking faults are also transferred from the core to both shells. The shell thickness differs between the sides and this observation is discussed in section 4.5.1.3.

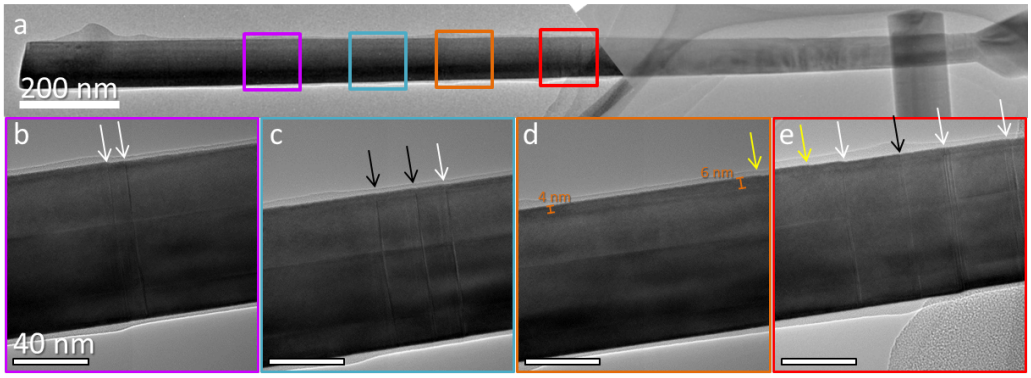

Figure 4.23: (a) A low-magnification TEM image of an InAs-GaSb-InAs core-shell-shell nanowire, (b-e) HRTEM images of the same nanowire. The colored boxes on the (a) low-mag TEM micrograph at the top indicate the origin of the HRTEM images. The white arrows mark the tapering of the outer shell in correlation with the stacking faults from the core, whereas the black arrows indicate the stacking faults which do not induce tapering. The yellow arrows indicate tapering of the outer shell not induced by a stacking fault. In the (d) the outer shell thickness is seen to increase in the growth direction. It can also be seen that the shell thicknesses differ on the different sides of the nanowire.

The HRTEM images of the core-shell-shell structure is shown in figure 4.23(a-e). The images revealed a general correlation between stacking faults of the core (and consequently the shell) and tapering of the outer shell 4.23(b-e). This was observed for the InAs-GaSb core-shell

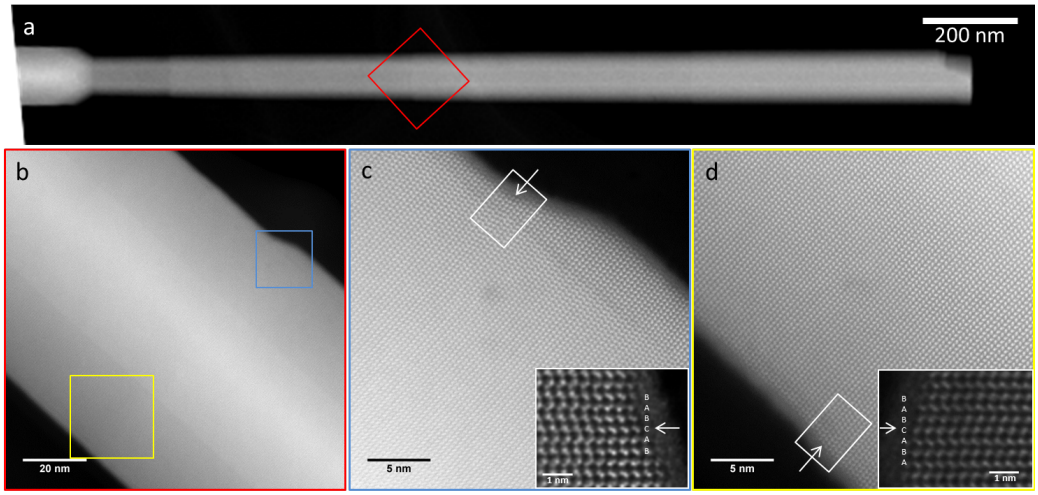

Figure 4.24: HAADF-STEM analysis showing a stacking fault which seem to have a correlation to the decrease in shell thickness. (a) The low magnification STEM image indicates the area from where the (b) overview STEM image is acquired. The blue and yellow boxes in (b) indicate the (c-d) HR-STEM image of the stacking fault on the two sides. The insets in (c-d) are the deconvolved images of the areas of interest with the stacking order marked. The white arrow indicates the single stacking fault.

nanowires and has been discussed in section 4.3.2.1. The same argument might be employed for this structure. However, there are several exceptions in which either the tapering steps occur with no stacking faults in the vicinity, or no tapering occurs at a stacking fault.

It was also observed at one point that the outer shell thickness is slightly increasing for a length of around 60 nm and ends with a step that decreases the thickness in no visible correlation with a stacking fault (Fig. 4.23d). This single event of a temporary increase in shell thickness contradicts the earlier discussion for the tapering effect of the core-shell structure. However, all other observations indicate that the shell tapers in the growth direction and hence this single event can be considered an anomaly.

Tapering of the outer InAs shell in correlation to a single stacking fault was observed in HAADF-STEM analysis and is presented in figure 4.24(a-d). It was observed that the shell did not taper equally on the visible sides of the nanowire (Fig. 4.24c, d). The stacking order with the stacking fault indicated is shown in figure 4.24(c, d) as well. Another tapering event of the outer InAs shell was observed by HAADF-STEM analysis, which is show in figure 4.25. The shell tapers without any visible relation to a stacking fault. The preserved WZ stacking order as well as the row where the tapering occurs is indicated in figure 4.25(b).

4.5.1.2 Chemical composition

High resolution EDX was performed on the double-shell structure and is presented in figure 4.26(a-b). The analysis provides elemental maps of O, In, As, Ga, and Sb (Fig. 4.26c, d, e, g, h, respectively). As aimed from the growth conditions the composition of the core is InAs, the thick inner shell is composed of GaSb and the thin outer shell is InAs (Fig. 4.26f). The core and the outer shell exhibit a confined signal from In and As; and the Ga and Sb signals are dispersed over the core and the inner shell structure. In fact this is due to the 3D structure of the nanowires. The GaSb shell covers the core and the signal over the core comes from the area overlapping with the shell. This signal is not at all present over the outer shell. Note that the In and As signals are very weak over the inner shell, as the outer shell is quite thin. A weak signal of O is detected from the outermost layer of the nanowire but is considered to originate from the organic contaminations covering the nanowires. No signal of the other elements is detected in that area which rejects the idea of having an oxide layer of any of the compounds (like Ga oxide in the case of InAs-GaSb core-shell nanowires).

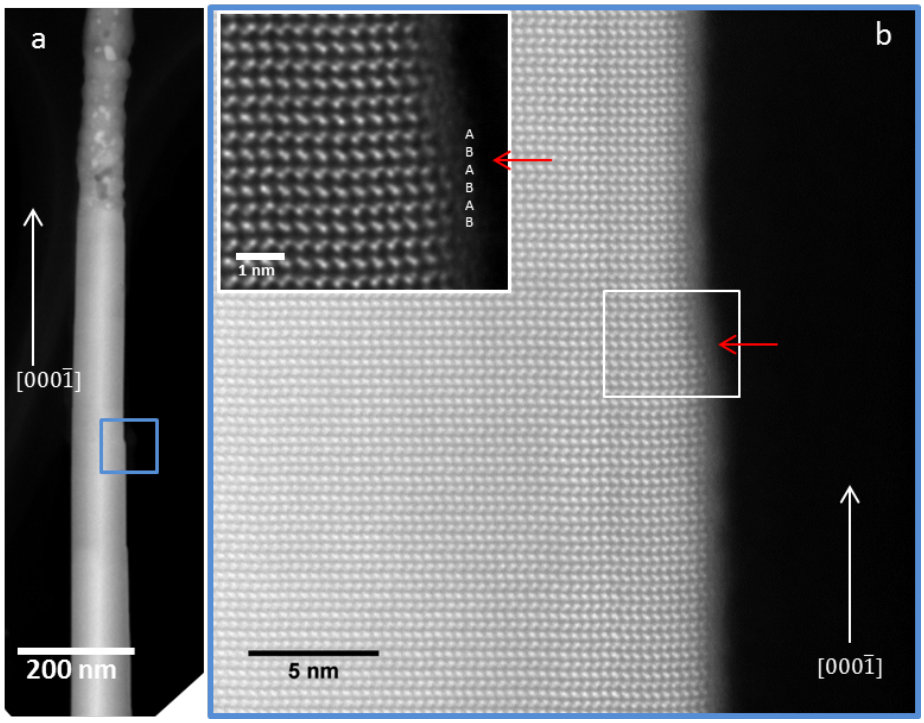

Figure 4.25: The image shows a InAs shell tapering event. The (a) STEM image of the nanowire shows the area from where the (b) HR-STEM image is aqcuired. A tapering event, marked with a red arrow can be seen in (b). The origin of the inset is marked with a white box in (b) and the stacking order as well as the red arrow which indicate the shell tapering event is indicated.

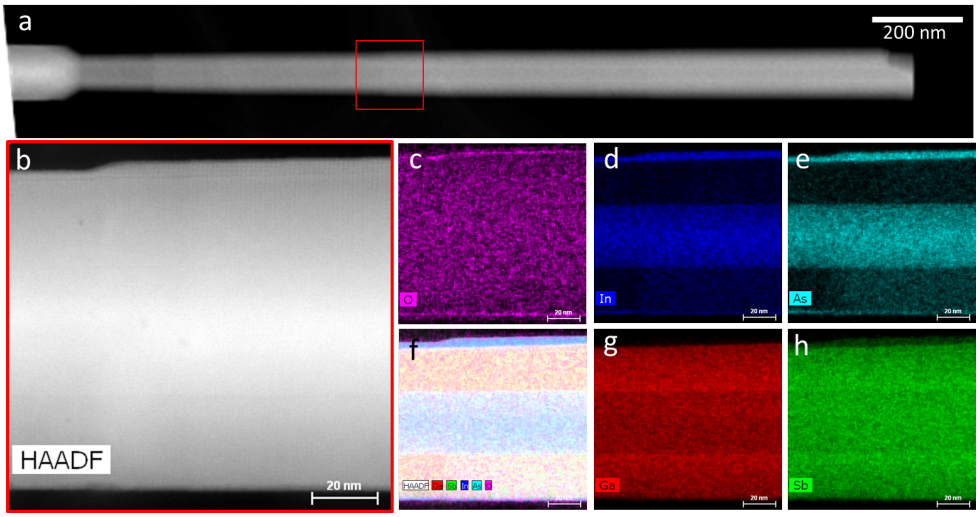

Figure 4.26: The elemental EDX analysis of the (a) core-shell-shell structure. (b) The STEM image marked the area the elemental mapping was performed. The EDX maps of (c) O, (d) In, (e) As, (g) Ga and (h) Sb signals. The image with all the signals overlaid is seen in (f).

4.5.1.3 Geometry

The thickness of the shell was found to differ between the sides in some nanowires, and to be uniform in others. This was observed for nanowires imaged on zone axis $[11\bar{2}0]$, as a clear interface contrast is not possible on the other zone-axis $[12\bar{3}0]$ (section 1.1.4.3). The contrast in the HAADF STEM image in fig 4.27(a) indicated a non-uniform morphology of the nanowire along the diameter. An intensity profile across the width of the wire did not reveal a hexagonal cross-section (Fig. 4.27b), which is the expected 3D structure of WZ nanowires. In the case of InAs-GaSb, the average atomic number (Z) of each compound is exactly the same. Therefore, in HAADF-STEM images the contrast change is only related to the thickness. The thicker area appears brighter in the STEM image and hence the intensity profile reveals the relative thickness across the nanowire. With this information we conclude that the cross-section of the nanowire is a truncated triangle (hexagonal shape with a 3-fold symmetry) instead of a symmetric hexagon. A scheme of this is presented in figure 4.27(c). This is further validated by an EDX line scan performed in the vicinity in which the intensity (counts) and broadness of Ga and Sb signals differ depending on the side (Fig. 4.27d). The left side have a lower (less counts) but broader signal and the right side have a higher signal over a shorter distance. This correlates to the cross-sectional illustration in where the left side have a thicker lateral thickness but thinner vertical thickness compared to the right side. If this nanowire was imaged on zone axis $[12\bar{3}0]$, which is perpendicular to $[11\bar{2}0]$, the intensity profile would appear symmetric. However, a sharp core-shell interface would not be seen in this zone axis in HRTEM or HR-STEM images.

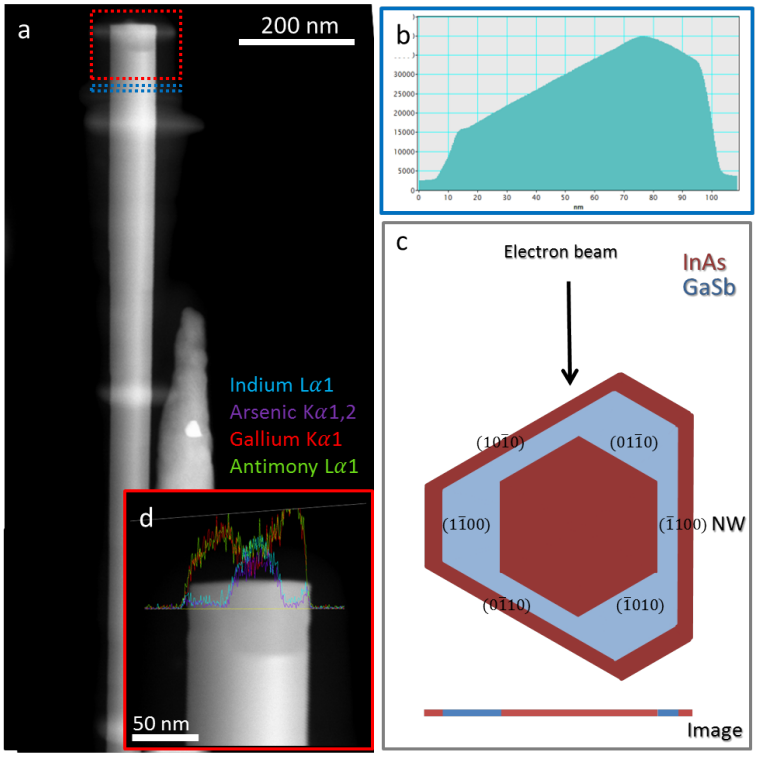

Figure 4.27: In the (a) STEM image to the left, the red box indicates where the (d) EDX line scan is acquired. The line scan reveals a higher signal from the shell on the right side which and a (b) intensity profile across the nanowire (blue in (a)) reveals the 3-fold symmetry of the shell. (c) An illustration of the triangular-truncated cross-sectional shape is illustrated below. The red and blue line under the hexagonal shape visualizes the core-shell-shell contrast in the STEM image.

In contrast, symmetric shells have also been observed. The HAADF STEM image of another nanowire (Fig. 4.28a) from the same sample show different shell dimensions than the nanowire shown previously(4.28). As mentioned before, the appearance of the shell can be due to the

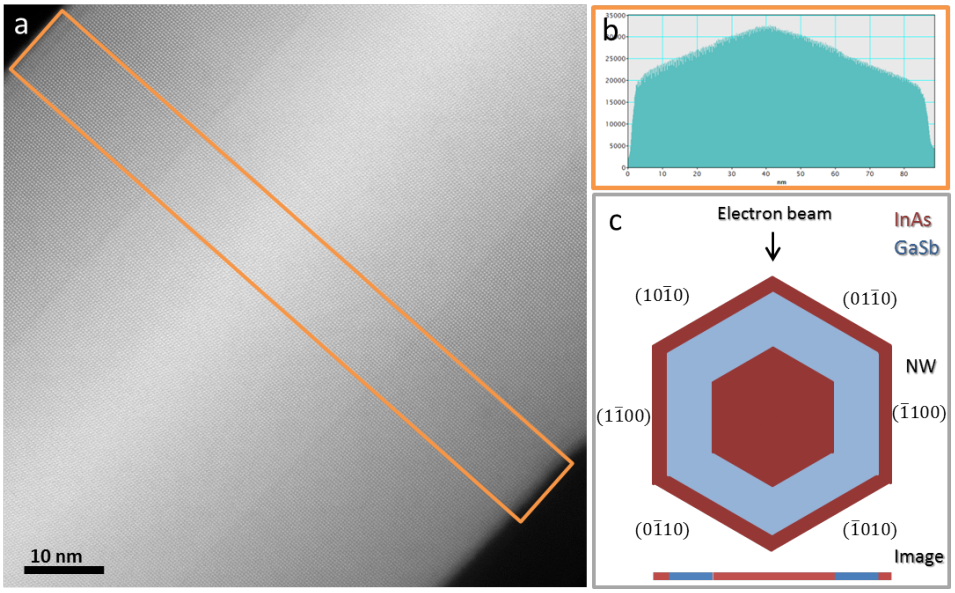

Figure 4.28: (a) A HAADF STEM image where the shell is seen to be of equal thickness on both sides of the core. The area from where (b) the intensity profile is acquired is marked in orange. (b) The intensity profile indicates the 6-fold symmetry shown and (c) the hexagonal cross-section of the nanowire is illustrated below. The red and blue line under the hexagonal shape visualizes the core-shell-shell contrast in the STEM image.

zone axis. From [12$\bar{3}$0] zone axis one could easily think that the 3-fold shells would appear symmetric. However, this is not the case. Firstly, from [12$\bar{3}$0] zone axis the dumbbell units would appear vertical (as shown in Fig. 1.7, chapter 1), and secondly it would not yield the strong interface contrast as we see in figure 4.28, as the lateral facets would not be along the zone axis (as shown in Fig. 1.8, chapter 1). The intensity profile over the width of the nanowire reveals a more symmetrical hexagonal shape rather than the truncated-triangular shape which is presented in figure 4.28(b). A comparison of the two structures is presented in image 4.29.

4.5.2 The radial interface

4.5.2.1 Misfit dislocations

Heterostructures of bulk material with a lattice mismatch usually cannot be grown defect-free. Nanowires however, are an interesting structure as they have been found to elastically compensate the strain between structures with relatively large lattice mismatch. Generally heterojunctions of nanowires with high mismatch can be grown axially as the strain can be compensated by lateral relaxation [49] . Plastic dislocations, such as misfit dislocations, occur as the dominating relaxation mechanism in bulk material such as thin films[50]. Theoretical models of axial and core-shell structures indicate that this kind of nanowire heterostructures can accommodate 5 to 10 times more strain than planar thin films [51].

The lattice mismatch of WZ InAs-GaSb is 1.15%. This means that at least 1 misfit dislocation per 100 atomic rows should be present to relax the strain. If no plastic relaxation defects are found, the structure can be assumed to elastically compensate the strain induced by the lattice mismatch. Here in our nanowires we have only found one misfit dislocation between of the InAs shells in all the acquired HRTEM and HR-STEM images.

A HRTEM image of the misfit dislocation is shown in figure 4.30. To verify the presence of a misfit dislocation a FFT of the HRTEM image is acquired. The (0001) planes, which are along the growth direction and the planes perpendicular to the zone axis [11$\bar{2}$], are filtered

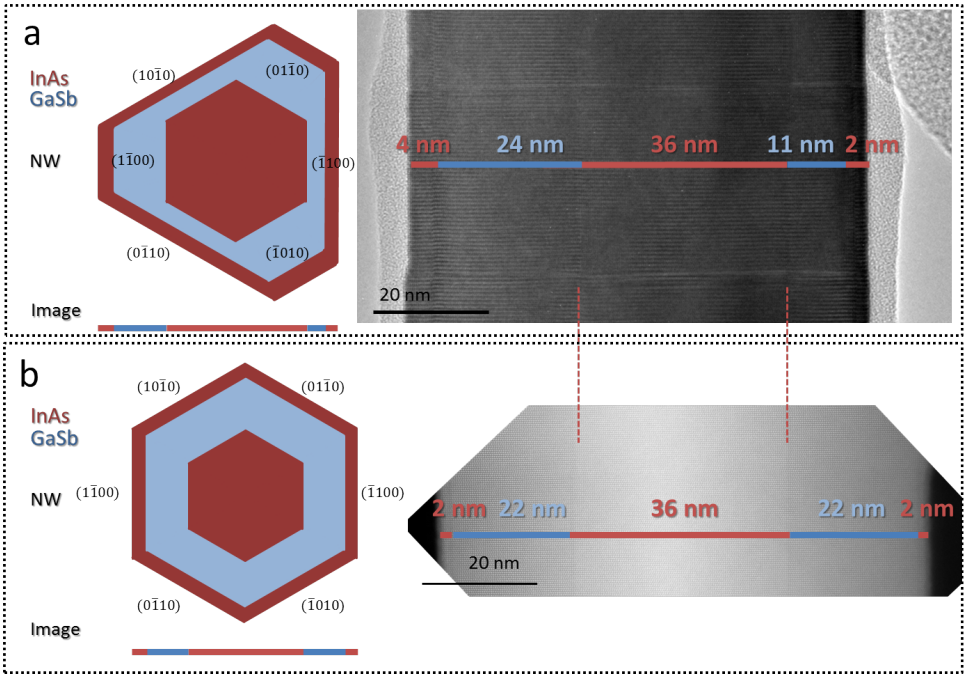

Figure 4.29: The figure shows two nanowires from with different appearances from the same sample. In (a) the triangular-truncated symmetry is illustrated with a corresponding HRTEM image of such a nanowire and in (b) the hexagonal structure is seen and a STEM image of the corresponding nanowire. The structures are comparable as the images are acquired on the same zone axis [11$\bar{2}$0]. The red dashed lines indicate that the thicknesses of the core are the same and when placed to overlap the difference in shell dimensions is clear.

and the inverse FFT results in an image of only the (0001) planes (Fig. 4.30b). By doing so the inset of an extra bilayer InAs could be seen. The reason is hence concluded to be due to compensation of the strain induced by the lattice mismatch. However since this was the only plastic relaxation found in the analyzed nanowires, it can be concluded that the structure, in most cases, elastically relaxes the lattice mismatched induced strain.

4.5.2.2 Composition and polarity

The double-shell structure was also examined by aberration corrected TEM. As in the InAs-GaSb core-shell structures, the radial interfaces appear darker as can be seen in figure 4.31. The darker interfaces are due to the Z-contrast and are first assumed to be composed of GaAs. This phenomena is further investigated by intensity profiles of the dumbbells visible in the atomic resolution HAADF STEM image (Fif. 4.32) and by taking the polarity into account.

The intensity profiles of the double shell structure reveal the polarity of the two shells. The polarity of the core could not be determined by this analysis as the GaSb shell is too thick to allow good contrast of the InAs core through the shell. However, from the reference sample (before the second shell) we assume the core to be As-polar which is the polarity inherited from the InAs (111) B substrates. The inner GaSb shell is Sb-polar and the InAs shell is In-polar. The interface is observed to have another composition and again we note that a polarity-inversion is not energetically favorable. Therefore, the interface is a mixture of As-polar InAs and GaAs (a ternary GaInAs). Note that this is only one bilayer at the radial interfaces.

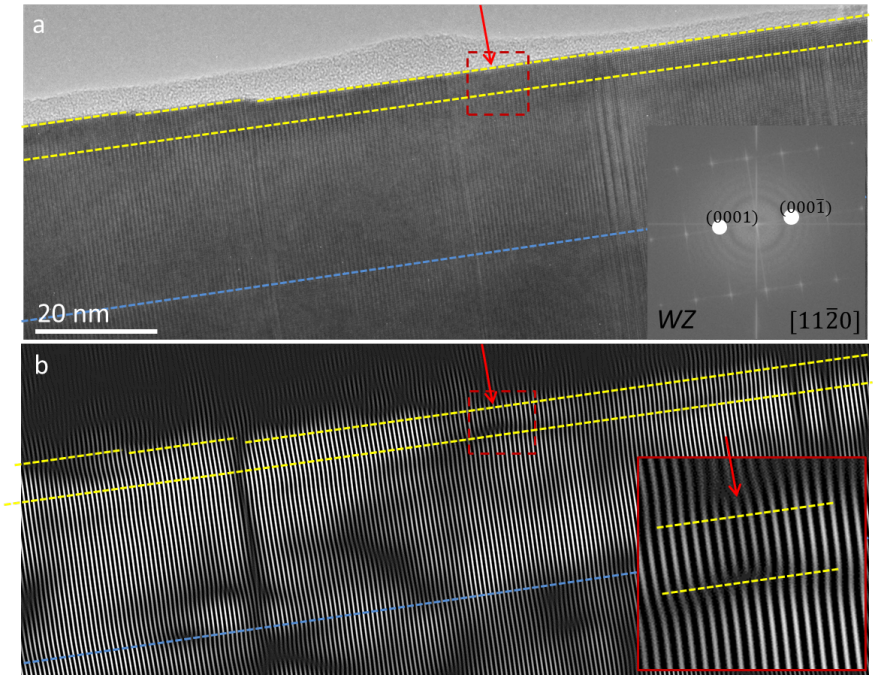

Figure 4.30: (a) A HRTEM image of a part of the core-shell-shell structure where both shells can be observed and from where the FFT is acquired. The area covers approximately 200 atomic rows. (b) The image is filtered by taking only (0001) plane reflections in the FFT and masking the rest (inversed FFT). The yellow dashed lines define the InAs shell and the blue line the InAs-GaSb core-shell interface. The red dashed box indicates the area where the misfit dislocation was found. The area magnified area of the misfit is shown as an inset in (b). The red arrow marks the misfit dislocation.

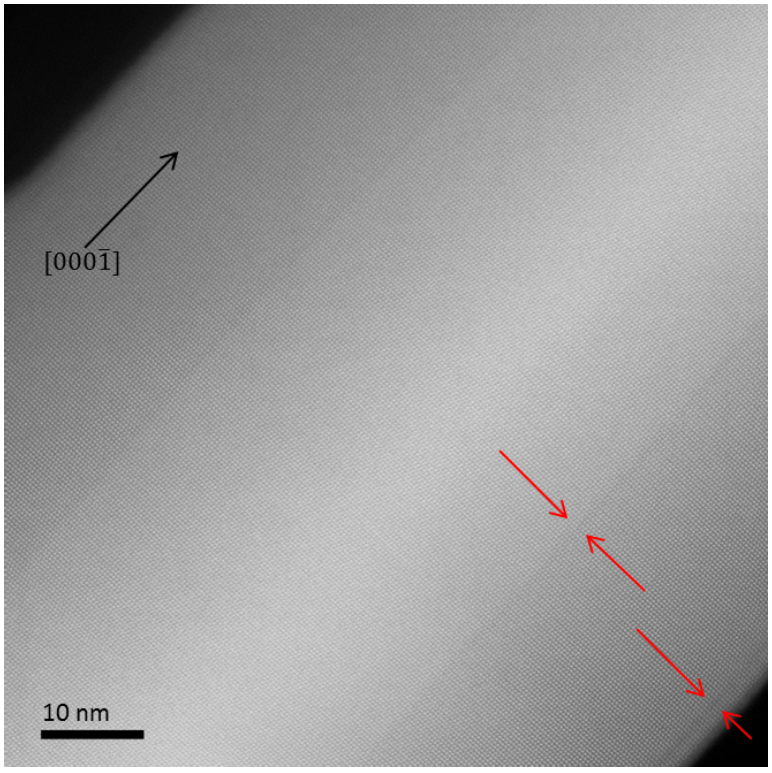

Figure 4.31: A HAADF-STEM image of the InAs-GaSb-InAs core-shell-shell structure. The red arrows note the darker interfaces of the InAs-Gasb core-shell and GaSb- InAs shell-shell. The black arrow denotes the growth direction.

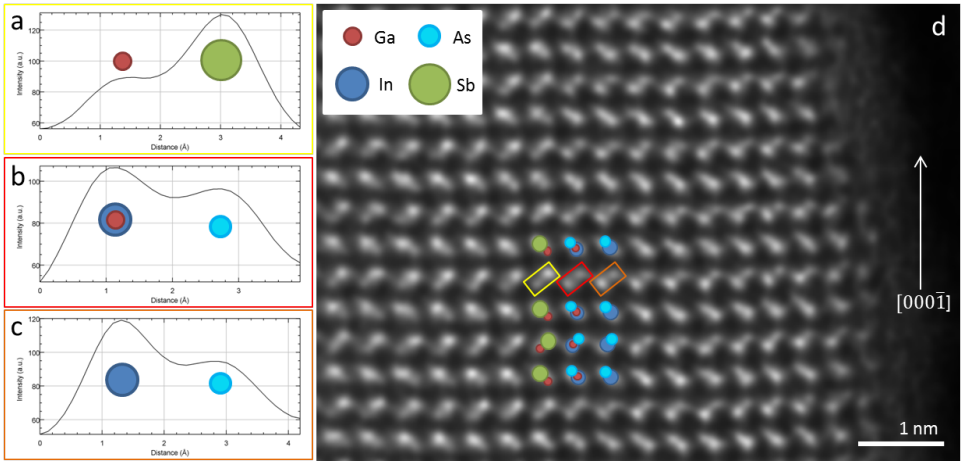

Figure 4.32: (a-c) The intensity profile of the dumbbells at the GaSb-InAs shell-shell interface are acquired from the (d) deconvolved atomic resolution HAADF STEM image. (a-c) show the intensity profile of one dumbbell unit in (d), the GaSb (a-yellow), the interface comprised of alternating GaAs and InAs (b-red) and the InAs (c-orange). The polarity is conserved throughout the shell-shell-interface. A step of the InAs shell can be observed and as well as it occurs without a visible relation to any type of defect.

4.5.3 The polycrystalline areas

Nanowires with a different morphology within the same sample were observed during TEM analysis and are shown in figure 4.33(a). HRTEM images were acquired on this part (one is shown in Fig. 4.33b) to investigate the crystal structure. The FFT (Fig. 4.33c) of the HRTEM images revealed a polycrystalline ZB structure overlapping with WZ in the center of the wire, while the 'shell' has a more uniform ZB structure except some twin planes. This indicates that the core has a WZ structure and the surrounding shells are of ZB structure.

This peculiar find evokes the question if this is an artefact from the growth or due to recrystallization after the growth. A similar kind of polycrystalline structure was observed and the EDX analysis (Fig. 4.34) reveals several interesting structural issues. Firstly, the presence of Au particles (Fig. 4.34c) on the polycrystalline area was observed. Secondly, the signal of In (Fig. 4.34d) is no longer confined to the core and outer shell, but spread over the GaSb inner shell as well. In contrast, the As, Ga and Sb signals (Fig. 4.34e, f, g) are somewhat still confined to their shell structures. Lastly, the core-shell-shell structure is observed to reappear after the polycrystalline area, in the growth direction.

It is speculated that the nanowires have deformed over time rather than during growth. This might have happened as there were several months between the growth and TEM characterization sessions. The deformed area could be due to the metastability of WZ resulting in a phase transformation to ZB in presence of Au nanoparticles, especially since the shell was found to be ZB while the core still had the WZ structure (Fig. 4.33). The nanowire analyzed with EDX regained its double shell structure after the deformed segment which is unlikely to happen during growth. Also that the composition appears to have change for the layers, as the signal from In is no longer confined to the core and outer shell, might also indicate a transformation after the growth. Why the gold is present is not clear but as it was only found on the deformed part this might play a role in the initiation of the structure transformation. If the Au particles were present during the growth it would probably have induced some branching growth which was not observed here, which further indicates some post-growth reconstruction.

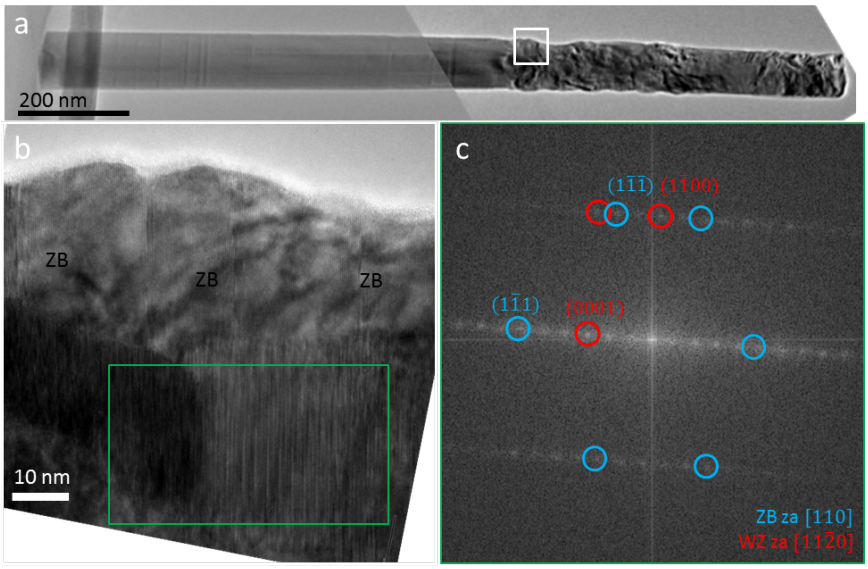

Figure 4.33: (a) A low magnification image of the core-shell-shell nanowire which exhibit a peculiar structure at the top, the white box indicate from where the (b) HRTEM image is acquired. The green box denotes from where the (c) FFT is calculated. The FFT of the moiré fringes visible in the green box in (b) reveals the diffraction pattern from WZ as well as ZB as indicated in the figure.

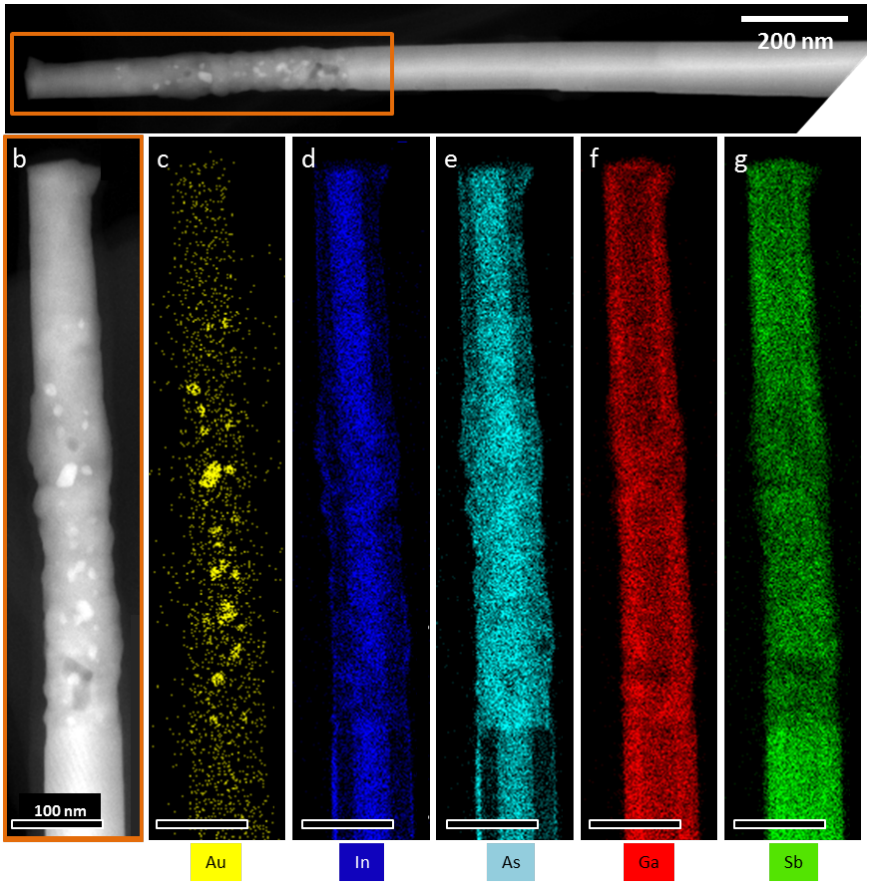

Figure 4.34: The EDX data from the polycrystalline area of a core-shell-shell nanowire (a) is presented in the figure. (b) A STEM image over the analyzed area. The polycrystalline area is located close to the axial segment (which is broken off) and the rest of the nanowire has the expected crystalline WZ core-shell-shell structure. The EDX maps for (c) Au, (d) In, (e) As, (f) Ga and (g) Sb are presented.

Chapter 5

Conclusion

The aim of the thesis was to give an advanced characterization and structural understanding of WZ InAs-GaSb heterostructured nanowires, by means of TEM and STEM imaging as well as EDX. The InAs-GaSb material is of interest due to its high charge carrier mobility, which has possible applications in electronic devices such as FETs. However, the previous studies have been on the system in ZB structure. GaSb has only recently been found to be able to form WZ structure. In this case only short WZ segments could be acquired on nanowire templates [22]. The nanowire core-shell structure in general is of interest as it forms a radial heterojunction which have a more efficient component volume and in addition have other applications than nanowires with axial heterojunctions. We have analyzed six different samples where the main focus laid on the InAs-GaSb core-(thin) shell and InAs-GaSb-InAs core-shell-shell nanowires. The structural and compositional characterization performed in this TEM study can be used to develop the growth parameters and further correlate to the electrical properties of the nanowires.

The TEM analysis revealed the morphology of the shell, which is the first observed WZ shell structure of GaSb. This is of importance for further structural development of GaSb in WZ structure as well as other III-V materials that have not exhibited polytypism before. An emphasis of this thesis laid on the radial and axial interfaces. Advanced characterization of these interfaces was performed by means of HR-STEM and high resolution EDX.

The study revealed tapering of the GaSb shell. This was attributed to diffusion limited shell growth and the presence of stacking faults of the core. From this it could be concluded that a higher mass flow of the shell precursors and a long growth time, compared to the growth parameters for synthesis of GaSb ZB, were essential in order to obtain the GaSb in WZ structure.

The shells observed in all nanowire samples were fully epitaxial and very few (one) misfit dislocations were found. This confirms that the lattice-mismatch of 1.15% of InAs and GaSb was small enough for the structures to elastically compensate the lattice-mismatch strain. This is promising for future development of InAs-GaSb heterostructured nanowires.

Different 3D structures of nanowires with a thick GaSb shell, within the same sample, were observed. Some nanowires had shells with different thicknesses depending on the side, while others had a uniform shell. Clear interface contrast of WZ structures on zone axis $[11\bar{2}0]$ and complementary intensity profiles of HAADF STEM micrographs revealed a 3-fold truncated-triangle and a 6-fold symmetric hexagonal shape of the GaSb shells. The latter is the expected 3D structure of WZ nanowires since all six lateral facets are equivalent. In addition, the ZB facets were found to induce shell growth differently; this is in correlation with previous studies of ZB where the six lateral facets are not equivalent [**polarity-driven-nonuniform-comp-in-inasga**][47].

The analysis with the aberration corrected TEM provided atomic resolution images of the crystal structure and composition. A one atomic bilayer thick ternary, GaInAs, was found

with this method at the radial interfaces. At the axial interface between the InAs core and the GaSb axial segment was a short (∼6 nm) GaAs-rich segment located. This short segment is concluded to originate from the reservoir effect of the seed particle during growth.

5.1 Outlook

The possible electronic application for InAs-GaSb heterostructures have been mentioned multiple times throughout the thesis. Follow-up electrical measurements are of high importance in order to gain knowledge of the electrical properties. In addition, the TEM investigations revealed peculiar structural issues, such as the presence of a ternary in the radial and axial interfaces, 3-fold and 6-fold symmetry of the shell geometry in the same sample and polycrystalline areas in some of the nanowire. Each of these issues can be further researched. In addition, the ternary may or may not affect the electrical properties of the nanowires and how it forms is of interest to understand in order to engineer the growth parameters accordingly. The appearance of the 3-fold and 6-fold symmetry would be interesting to understand as well as it may affect the performance in future devices. The polycrystalline areas are suspected to form after growth and this is of importance to investigate this further as compound stability usually is desired for electronic and optoelectronic compounds.

Appendix A

Phase contrast

Phase contrast is the dominating contrast in HRTEM imaging where the atomic columns of a crystalline material can be resolved. In order to understand the origin of phase contrast, does the contrast transfer function (CTF)need to be described first.

A.0.1 The contrast transfer function (CTF)

The contrast transfer function (CTF) describes mathematically the information that is transmitted from the specimen to the image in TEMs. The CTF is the Fourier transform of the point spread function $h(x, y)$ and is given by the relation

$$G(\boldsymbol{u}) = F(\boldsymbol{u})H(\boldsymbol{u}), \tag{A.1}$$

where $G(\boldsymbol{u})$ is the Fourier transform of $g(x, y)$ which is the function of the extended region in the image that corresponds to the point (x, y) in the specimen. $F(\boldsymbol{u})$ is the Fourier transform of the specimen function $f(x, y)$ and $\boldsymbol{u}$ is the reciprocal lattice vector that corresponds to (x, y). $H(\boldsymbol{u})$ depends on the respective function of the apertures in the TEM ($A(\boldsymbol{u})$), the aberration of the lenses ($B(\boldsymbol{u})$) and the attenuation of the wave (the envelope function $E(u)$). The contrast transfer function can then be written as

$$H(\boldsymbol{u}) = A(\boldsymbol{u})E(\boldsymbol{u})B(\boldsymbol{u}), \tag{A.2}$$

The aberration function $B(\boldsymbol{u})$ can be expressed as

$$B(\boldsymbol{u}) = e^{ix(\boldsymbol{u})}. \tag{A.3}$$

The term $x(\boldsymbol{u})$ can be described as a function of the microscopes' spherical aberration c_s, the wavelength of the incident electrons, λ and the defocus Δf and can be written as

$$x(\boldsymbol{u}) = {}^1\!/_2 C_s \pi \lambda^3 \boldsymbol{u}^4 + \pi \lambda \Delta f \boldsymbol{u}^2. \tag{A.4}$$

The details about the mathematics behind these functions are beyond the scope of this thesis but well represented in the literature [33]. However, $x(\boldsymbol{u})$ is an important concept which is needed for understanding the limits of the microscopes spatial resolution with parameters that are known or variable. This function is important in order to achieve high resolution images which will be described next. [33]

A.0.2 Phase contrast function (pCTF)

In HRTEM imaging is it of desired to operate in a regime where the amplitude change of the waves are negliglbe and the phase change dominating. One of the requirements for making use of phase contrast imaging is that the specimen is single crystalline or thin enough so the electrons only interact with the specimen (atom or atomic column) once. This allows using the weak phase-object approximation (WPOA) which states that the transmitted wave function's amplitude will be linearly related to the projected potential of the specimen [33]. The WPOA results in that the transfer function of the HRTEM is the CTF (eq. A.2) without the envelope function $E(\boldsymbol{u})$, as the envelope function corresponds to the amplitude contrast contribution. The WPOA also resolve that it is only the imaginary part of the aberration function $B(\boldsymbol{u})$ that contributes to the intensity and therefore $B(\boldsymbol{u})$ can be rewritten as

$$B(\boldsymbol{u}) = 2\sin x(\boldsymbol{u}). \tag{A.5}$$

The contrast transfer function can then be described as

$$H(\boldsymbol{u}) = A(\boldsymbol{u})B(\boldsymbol{u}) = A(\boldsymbol{u}) \cdot 2\sin x(\boldsymbol{u}). \tag{A.6}$$

$A(\boldsymbol{u})$ is the aperture function and by assuming that the astigmatism can be properly corrected the contrast transfer function for HRTEM are just multiples of a sinusoidal term. $x(\boldsymbol{u})$ (same as eq. A.4) can be described as a function of the microscopes spherical aberration C_s, the wavelength of the incident electrons, λ, and the defocus, Δf, and expressed as

$$x(\boldsymbol{u}) = {}^1\!/_2 C_s \pi \lambda^3 \boldsymbol{u}^4 + \pi \lambda \Delta f \boldsymbol{u}^2. \tag{A.7}$$

The transfer function as a function of $\boldsymbol{u}$ (reciprocal lattice vector nm^{-1}) can be plotted to visualize the TEM's highest spatial resolution which is where the first cross over ($\sin x = 0$) in the graph is located (see figure A.1). This value can be varied by changing the parameters in $x(\boldsymbol{u})$ and is optimized when the cross over is at the highest value of $\boldsymbol{u}$. Since C_s is a fixed value for most TEMs (including LU's JEOL 3000F) and the microscope's highest possible acceleration voltage gives the shortest wavelength, the only variable parameter is the defocus value. The optimization of $x(\boldsymbol{u})$ is done by using the so called Scherzer defocus[52], which is the optimized negative defocus that can be calculated with equation

$$F_{Scherzer} = -1.2\sqrt{C_s \lambda}, \tag{A.8}$$

which balances the spherical aberrations of the microscope and wavelength of the electrons to achieve the highest spatial resolution possible with the specific microscope according to the equation ($x(\boldsymbol{u})$).

The point resolution is then given by equation

$$R_{Scherzer} = 0.66 \cdot C_s^{1/4} \cdot \lambda^{-3/4}. \tag{A.9}$$

[33]

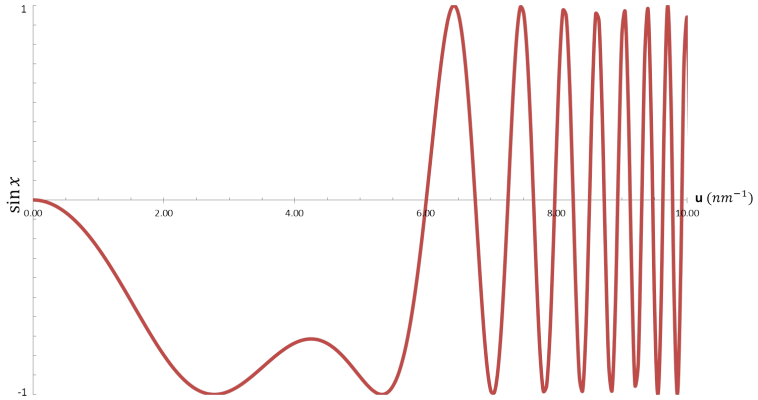

Figure A.1: The phase contrast transfer function $\sin(x(u))$ vs $\boldsymbol{u}$. The first cross-over indicates the highest spatial resolution with the standard parameters (C_s, λ) for JEOL 3000F operating at the Scherzer focus.

Bibliography

[1] Hideki Gotoh Guoqiang Zhang Kouta Tateno and Tetsuomi Sogawa. "Towards New Low-dimensional Semiconductor Nanostructures and New Possibilities". In: *NTT Technical Review* 8.8 (2010).

[2] Guozhen Shen and Di Chen. "One-dimensional nanostructures for electronic and optoelectronic devices". In: *Frontiers of Optoelectronics in China* 3 (2010).

[3] Yat Li et al. "Nanowire electronic and optoelectronic devices". In: *Materials today* 9 (2006).

[4] Donald A Neamen. *Semiconductor physics and devices*. McGraw-Hill Higher Education, 2003.

[5] Günter Grossman. *Fasta Tillståndets Fysik - Kompendium*. Fasta Tillståndets Fysik Lunds Universitet, 2013.

[6] Udo W Pohl. *Epitaxy of Semiconductors: Introduction to Physical Principles*. Springer Science & Business Media, 2013.

[7] XL Chen et al. "Radial growth dynamics of nanowires". In: *Journal of crystal growth* 222.3 (2001), pp. 586–590.

[8] VG Dubrovskii et al. "Shape modification of III-V nanowires: The role of nucleation on sidewalls". In: *Physical Review E* 77.3 (2008), p. 031606.

[9] Mohanchand Paladugu et al. "Evolution of wurtzite structured GaAs shells around InAs nanowire cores". In: *Nanoscale research letters* 4.8 (2009), p. 846.

[10] Reza Zamani. "Structure Nanoengineering of Functional Nanomaterials: Advanced Electron Microscopy Study". PhD thesis. Universitat de Barcelona, 2014.

[11] Philippe Caroff et al. "Controlled polytypic and twin-plane superlattices in III–V nanowires". In: *Nature nanotechnology* 4.1 (2009), pp. 50–55.

[12] Maria De La Mata et al. "Polarity assignment in ZnTe, GaAs, ZnO, and GaN-AlN nanowires from direct dumbbell analysis". In: *Nano letters* 12.5 (2012), pp. 2579–2586.

[13] JW Faust Jr and A Sagar. "Effect of the Polarity of the III-V Intermetallic Compounds on Etching". In: *Journal of Applied Physics* 31.2 (1960), pp. 331–333.

[14] Fabian Schuster et al. "p-GaN/n-ZnO heterojunction nanowires: optoelectronic properties and the role of interface polarity". In: *ACS nano* 8.5 (2014), pp. 4376–4384.

[15] Bahram Ganjipour et al. "Carrier control and transport modulation in GaSb/InAsSb core/shell nanowires". In: *Applied Physics Letters* 101.10 (2012), p. 103501.

[16] Tim Oliver Stadelmann. "Antidot superlattices in InAs-GaSb double heterostructures: transport studies". PhD thesis. University of Oxford, 2006.

[17] Bahram Ganjipour et al. "High current density Esaki tunnel diodes based on GaSb-InAsSb heterostructure nanowires". In: *Nano letters* 11.10 (2011), pp. 4222–4226.

[18] Anil W Dey et al. "High-current GaSb/InAs (Sb) nanowire tunnel field-effect transistors". In: *IEEE Electron device letters* 34.2 (2013), pp. 211–213.

[19] Martin Ek et al. "Formation of the axial heterojunction in GaSb/InAs (Sb) nanowires with high crystal quality". In: *Crystal Growth & Design* 11.10 (2011), pp. 4588–4593.

[20] Bahram Ganjipour et al. "Electrical properties of GaSb/InAsSb core/shell nanowires". In: *Nanotechnology* 25.42 (2014), p. 425201.

[21] Luna Namazi et al. "Selective GaSb radial growth on crystal phase engineered InAs nanowires". In: *Nanoscale* 7.23 (2015), pp. 10472–10481.

[22] Sepideh Gorji Ghalamestani, Sebastian Lehmann, and Kimberly A Dick. "Can antimonide-based nanowires form wurtzite crystal structure?" In: *Nanoscale* 8.5 (2016), pp. 2778–2786.

[23] Kimberly A Dick et al. "Control of III–V nanowire crystal structure by growth parameter tuning". In: *Semiconductor Science and Technology* 25.2 (2010), p. 024009.

[24] G.H. Döhler. "Electron-hole subbands at the GaSbInAs interface". In: *Surface Science* 98.1 (1980), pp. 108 –116.

[25] Herbert Kroemer. "The 6.1 A family (InAs, GaSb, AlSb) and its heterostructures: a selective review". In: *Physica E: Low-dimensional Systems and Nanostructures* 20.3 (2004), pp. 196–203.

[26] MP Mikhailova, KD Moiseev, and Yu P Yakovlev. "Interface-induced optical and transport phenomena in type II broken-gap single heterojunctions". In: *Semiconductor science and technology* 19.10 (2004), R109.

[27] Siyuranga O Koswatta, Steven J Koester, and Wilfried Haensch. "On the possibility of obtaining MOSFET-like performance and sub-60-mV/dec swing in 1-D broken-gap tunnel transistors". In: *IEEE Transactions on electron devices* 57.12 (2010), pp. 3222–3230.

[28] Jan G Gluschke et al. "Characterization of Ambipolar GaSb/InAs core–shell nanowires by thermovoltage measurements". In: *ACS nano* 9.7 (2015), pp. 7033–7040.

[29] Marc De Graef and Michael E McHenry. *Structure of materials: an introduction to crystallography, diffraction and symmetry*. Cambridge University Press, 2007.

[30] Lund University. *MAX IV and ESS*. 2016. URL: `http://www.lunduniversity.lu.se/research/max-iv-and-ess` (visited on 12/23/2016).

[31] Ake Hjelm. *Ett mikroskop i varldsklass*. 2011. URL: `http://liu.se/forskning/forskningsnyheter/1.298749?l=sv` (visited on 12/23/2016).

[32] MR Lee. "Transmission electron microscopy (TEM) of Earth and planetary materials: A review". In: *Mineralogical Magazine* 74.1 (2010), pp. 1–27.

[33] David B Williams and C Barry Carter. In: *Transmission electron microscopy*. Springer, 2009.

[34] Rik Brydson. *Aberration-corrected analytical transmission electron microscopy*. Vol. 3. John Wiley & Sons, 2011.

[35] Crispin Hetherington. "Aberration correction for TEM". In: *Materials Today* 7.12 (2004), pp. 50–55.

[36] Vincenzo Grillo and Francesca Rossi. "STEM_CELL: A software tool for electron microscopy. Part 2 analysis of crystalline materials". In: *Ultramicroscopy* 125 (2013), pp. 112–129.

[37] Toru Akiyama et al. "An empirical potential approach to wurtzite–zinc-blende polytypism in group III–V semiconductor nanowires". In: *Japanese journal of applied physics* 45.3L (2006), p. L275.

[38] Torsten Rieger et al. "Crystal phase selective growth in GaAs/InAs core–shell nanowires". In: *Crystal Growth & Design* 14.3 (2014), pp. 1167–1174.

[39] MC Plante and RR LaPierre. "Au-assisted growth of GaAs nanowires by gas source molecular beam epitaxy: Tapering, sidewall faceting and crystal structure". In: *Journal of Crystal Growth* 310.2 (2008), pp. 356–363.

[40] Ya-Nan Guo et al. "Polarity-driven nonuniform composition in InGaAs nanowires". In: *Nano letters* 13.11 (2013), pp. 5085–5089.

[41] Daniele Ercolani et al. "Growth of InAs/InAsSb heterostructured nanowires". In: *Nanotechnology* 23.11 (2012), p. 115606.

[42] Martin C Plante and Ray R LaPierre. "Analytical description of the metal-assisted growth of III–V nanowires: axial and radial growths". In: *Journal of Applied Physics* 105.11 (2009), p. 114304.

[43] Kimberly A Dick et al. "Crystal phase engineering in single InAs nanowires". In: *Nano letters* 10.9 (2010), pp. 3494–3499.

[44] Hannah J Joyce et al. "Phase perfection in zinc blende and wurtzite III- V nanowires using basic growth parameters". In: *Nano letters* 10.3 (2010), pp. 908–915.

[45] Jonas Johansson et al. "Diameter dependence of the wurtzite- zinc blende transition in InAs nanowires". In: *The Journal of Physical Chemistry C* 114.9 (2010), pp. 3837–3842.

[46] Muhammad Iqbal Bakti Utama et al. "Twinning-, Polytypism-, and Polarity-Induced Morphological Modulation in Nonplanar Nanostructures with van der Waals Epitaxy". In: *Advanced Functional Materials* 23.13 (2013), pp. 1636–1646.

[47] Reza R Zamani et al. "Polarity-driven polytypic branching in Cu-based quaternary chalcogenide nanostructures". In: *ACS nano* 8.3 (2014), pp. 2290–2301.

[48] Frank Glas, Jean-Christophe Harmand, and Gilles Patriarche. "Nucleation antibunching in catalyst-assisted nanowire growth". In: *Physical review letters* 104.13 (2010), p. 135501.

[49] Elif Ertekin et al. "Equilibrium limits of coherency in strained nanowire heterostructures". In: *Journal of Applied Physics* 97.11 (2005), p. 114325.

[50] Huajian Gao. "Some general properties of stress-driven surface evolution in a heteroepitaxial thin film structure". In: *Journal of the Mechanics and Physics of Solids* 42.5 (1994), pp. 741–772.

[51] Karen L Kavanagh. "Misfit dislocations in nanowire heterostructures". In: *Semiconductor Science and Technology* 25.2 (2010), p. 024006.

[52] O Scherzer. "The theoretical resolution limit of the electron microscope". In: *Journal of Applied Physics* 20.1 (1949), pp. 20–29.